Microstructures, mineral chemistry and geochronology of white micas along a retrograde evolution: An example from the Aar massif (Central Alps, Switzerland)

Alfons Berger[1,*], Philip Wehrens[1,2], Pierre Lanari[1], Horst Zwingmann[3], Marco Herwegh[1]

[1]: Institut für Geologie, Universität Bern, Baltzerstr. 1+3, CH-3012 Bern, Switzerland
[2]: now at Swisstopo, Seftigenstr. 264, CH-3084 Wabern, Switzerland
[3]: Division of Earth and Planetary Sciences, Graduate School of Science, Kyoto University, Sakyo-ku, Kyoto, 606-8502, Japan.

*: corresponding author:
alfons.berger@geo.unibe.ch
Tel: ++41-31-6314990

Abstract

This study investigates gneissic tectonites of different mechanical origins, and aims at unravelling the link between microstructures, white mica chemistry and K-Ar data. The highest temperature mylonitic deformation, which is investigated, is dominated by dislocation creep in monomineralic quartz, and viscous granular flow in polymineralic domains. These mylonites show homogenous mineral chemistry, resulting in robust and consistent K-Ar age data. The lowest temperature deformation investigated, is that of a retrograde brittle deformation, producing cohesionless fault gouges. Within the cohesionless fault gouges, frictional granular flow is considered as the main deformation mechanism. The K-bearing phases inside the fault gouges record no chemical resetting during this brittle overprint, but contain mechanically fragmented K-bearing micas and significant amounts of newly produced smectite. This yields K-Ar ages inside of a gouge that are in the range of adjacent mylonite ages, and may not represent the timing of gouge formation. In an effort to understand these uncertainties in K-Ar ages, detailed observations of the microstructural context of K-bearing white mica were made. Microstructural criteria in combination with quantitative element mapping allowed for the discrimination of five important mica-related processes: (1) fracturing/recrystallization of white mica; (2) (re)-precipitation of new fine-grained white mica inside the deforming rock matrix; (3) pseudomorphic replacement of precursor minerals by white mica and chlorite; (4) pseudomorphic replacement of pre-existing white mica without grain size reduction; and (5) remnant grains. The combination of these different processes led to a high variability in mineral chemistry and isotope data for tectonites, which relates directly to variations in the size of the equilibrium volumes. Despite the samples being highly deformed in the presence of fluids, inherited sheet silicates may survive. If inherited sheet silicates are present they contribute to an increase in both the chemical heterogeneity and the apparent K-Ar ages of a sample.

Keywords: *white mica, microstructures, fault gouge, mylonite, K-Ar dating*

1 Introduction

Detailed knowledge of chemical and isotopic equilibrium is essential for the reconstruction of temperature-time paths. In this context, the use of chronometers and thermometers depends on the identification of equilibrium volumes and their correlation to specific geological events. The identification of such equilibration volumes is related to the system of interest (e.g., mineral-chemistry, isotopic data, fluid/rock-equilibrium, etc.) and in many cases local bulk and mineral compositions are used to model such equilibria (e.g., Vidal et al. 2006; Agard et al. 2010; Lanari et al., 2012; Lanari and Engi, 2017). In general, larger equilibrium volumes are reported at higher temperatures, in the presence of fluids and in highly deformed rocks (e.g., Wintsch, 1985; Carlson, 2010; Hobbs et al., 2010). These parameters are not independent, because many re-equilibration processes (i.e., deformation, inter- and intragranular diffusion, pseudomorphic replacement by dissolution-precipitation) are closely linked to temperature and fluid availability (Airaghi et al. 2017). In low-temperature deformation regimes, a high partitioning occurs between brittle quartz-feldspars and viscous deforming sheet silicates. Therefore, the identification of equilibrium volumes is important for pressure-temperature-time estimates. This is well investigated for higher-grade metamorphic conditions using characteristic metamorphic minerals. This study focuses on white micas, which are ubiquitous minerals present over a large temperature interval from amphibolite facies down to very-low-grade conditions (Dubacq et al. 2010 and references therein). They are also of special importance as they strongly influence the rheology of fault rocks (e.g., Faulkner et al., 2010).

Knowledge of equilibration volumes requires precise data on mineral-chemistry in order to identify iso-chemical volumes and to reconstruct physio-chemical conditions (e.g., McAleer et al., 2017; Scheffer et al., 2016; Cantarero et al., 2014; Lanari et al., 2012). In this study, we limit ourselves to the description of sheet-silicates. This mineral group is important as a thermo-barometer (e.g., Vidal and Parra, 2000; Parra et al., 2002; Dubacq et al., 2010) and is useful for dating by the Ar-system (e.g., Reichenbach and Rich, 1969; Kelley, 1988; Villa, 1998; van der Pluijm et al., 2001; Mulch et al., 2002; Rolland et al., 2009; Zwingmann et al., 2010; Sanchez et al., 2011; Derkowski et al., 2014; Lanari et al. 2014b; Kellett et al., 2016; Viola et al. 2016; Mancktelow et al., 2016). The link between microstructures, chemical and isotopic data provides insights in potential equilibrium volumes.

For this purpose, the well-investigated Aar-massif (Central Alps, Switzerland; e.g., Wehrens et al., 2016, 2017; Rolland et al. 2009; Challandes et al., 2008; Kammer, 1989) was utilized as a natural laboratory to investigate a link between microstructures, chemical and isotopic data and equilibrium volumes. The Aar-massif has a large distribution of strain and within the exhumed mid-crustal basement there are preserved different tectonites (mylonites, cataclasites and fault gouges). A complementary workflow of, quantitative element mapping, grain size sensitive isotope analysis and SEM-based microstructural investigations were applied to a suite of tectonites samples from upper greenschist-facies mylonites to cohesionless fault gouges. In addition, the results from equilibrium assumptions were compared with independent geological information. Furthermore, the use of structural overprinting relationships provided an independent data set, allowing for the reconstruction of a relative temperature-deformation (T-D) path.

2 Geological setting and structural inventory

The Aar massif is one of the largest external massifs of the Alps. It is mainly composed of pre-Variscan polymetamorphic gneisses, which were intruded by post-Variscan granitoids (Labhart, 1977; Abrecht, 1994; Schaltegger, 1994). At the Northern boundary these basement rocks are in contact with autochthonous cover consisting of a Mesozoic sedimentary sequence. The valley “Haslital” in the center of the Aar massif transects through all these different units (Figs. 1 and 2).

Multiple stages of deformation, from Ordovician to Alpine, affected the pre-Variscan basement rocks (Stalder, 1964; Steck 1968; Schaltegger, 1993; Schaltegger et al., 2003). Within the post-Variscan intrusives only Alpine deformation has been detected. An Alpine deformation and metamorphic gradient was proposed from north to south (e.g., Frey et al., 1980; Choukroune and Gapais, 1983; Bambauer et al., 2005; Wehrens et al., 2017). The north is characterized by lowest greenschist facies metamorphism, whereas in the south upper greenschist facies conditions prevailed (Bambauer et al., 2005; Bousquet et al., 2012; Challandes et al., 2008; Frey and Ferreiro Mählmann, 1999; Goncalves et al., 2012). The Alpine deformation in the Haslital section of the Aar-massif can be subdivided into four major deformation stages (Figs. 1 and 2; Wehrens et al., 2017): (1) Handegg-, (2) Oberaar-, (3) Pfaffenchopf-, and (4) Gadmen-deformation. The Handegg-deformation is present over the complete section of the Aar massif and is characterized by steep-reverse faulting (Fig. 2; Herwegh et al. 2017; Wehrens et al., 2016, 2017; Rolland et al., 2009; Kammer, 1989; Steck, 1968). These are dominant SW-NE striking steep

reverse/normal shear zones and faults with down-dip lineations. The Handegg structures can be well characterized in the post-Variscan plutons. These shear zones show subgrain-rotation recrystallisation in quartz and newly formed white mica in the intermediate and high temperature range (Wehrens et al., 2017; Rolland et al., 2009; Bambauer et al., 2009). The Handegg shear zones in the central and southern part of the massif cover temperatures in the stability field of biotite, but are also active to lower temperatures. In the southern area, the Handegg deformation is overprinted by the Oberaar deformation. This deformation is characterized by ductile strike-slip deformation (e.g., Rolland et al., 2009). In addition, the Pfaffenchopf deformation crosscut the Handegg shear zones in the northern Aar-massif (Fig. 2). The Pfaffenchopf structures are characterized by more moderately south dipping thrust planes (Fig. 2; Herwegh et al., 2014, 2017; Kammer, 1989; Labhart, 1966). The Pfaffenchopf deformation affects basement and Mesozoic sediments, which result in local carbonate mylonites that show dynamic recrystallization of calcite. In the basement, the shear zones and schistosity are characterized by the frictional-viscous transition. In most examples quartz deformed in a brittle manner, but in some cases local bulging recrystallization can be inferred. The main processes are re/neo-crystallization of white mica and chlorite. The Gadmen-structures are represented by brittle faults, gouges and a weak brittle schistosity. They crosscut the Handegg- and Pfaffenchopf-deformation, and in the northern area the fault gouges have been investigated in underground facilities. In the area further south, brittle deformation is also frequent, but the crosscutting relationship to the older deformation is not clear. Some of the brittle structures may also represent continuous deformation of the Handegg- and/or Oberaar deformation.

It is the P-T variations with time, across of the northern and southern regions of the Haslital area, that are key to understanding recrystallization processes and potential Ar-loss in mica. The southern Aar-massif is well investigated and peak P-T conditions of ~450°C and 6kbar are established there (Goncalves et al., 2012). This is consistent with δO^{18} thermometery (Fourcade et al., 1989) and observations of the transition from microcline to sanidine (Bambauer et al., 2005). The central part of the Aar-massif represents the transition between maximal temperatures of 450°C to the very low-grade conditions at the northern border (see below). This transition is characterized by the “biotite-in” and the “stilpnomelan-out” isograde (Steck and Burri, 1971; Niggli and Niggli, 1965; Jäger et al., 1961). From these conditions in the center, a steep gradient developed toward the northern end of the massif (Fig. 2). The northern rim is related to a lower maximal temperature of 250-300 °C and a

pressure in the range of 2-3 kbar (Frey et al., 1980). The samples selected for this investigation are from south of the “biotite-in” isograde (Fig. 1).

3 Sample location and description

Samples from mylonites to fault gouges are located along the above described temperature gradient (Figs. 1, 2 and Table 1). The tectonites can be subdivided into three major groups: (1) intermediate temperature granitoid mylonites, which are dominated by dislocation creep in quartz layers and viscous granular flow in polymineralic domains; (2) gneissic low temperature mylonites, in which there is the brittle deformation of quartz and feldspar and viscous deformation of sheet silicates; and (3) cohesionless fault gouges which are the product of brittle deformation. Along the deformation-temperature gradients, mineralogy, grain size and deformation mechanisms changed (Figs. 2 and 3).

The dominant deformation mechanisms are also connected to different deformation stages (see section 2; Fig. 2). The mylonite samples are located in the Central Aar-granite (Fig. 1). Sample GRS05 is related to Handegg deformation and involves dislocation creep in quartz layers and viscous granular flow in a compositionally mixed matrix. At the sample-location the shear zone consists of a 50 cm wide mylonite with a strain gradient toward the undeformed Central Aar granite. The shear zone can be traced for several kilometers along strike. Sample GRS06 originates from a nearby strike slip shear zone of several meters width and kilometers length (Table 1). The schistose host rock is cut by intercalations of bands of (i) mylonitic quartz and (ii) quartz-white mica (Fig. 4). These bands inside the host developed due to hydrothermal activity and are interpreted as synkinematic veins. The host-rock has a granitic composition for these mylonites. To some degree a polymineralic fine-grained matrix has developed consisting of recrystallized quartz, mica, and feldspar. There is a preferentially alignment of both white mica and biotite. Dynamically recrystallized grain sizes in the pure quartz bands and the schistose granitoid are comparable. In contrast, the white mica-quartz bands consist of newly formed white mica with grain sizes down to 3 µm (Fig. 4). Handpicked large micas originate from the schistose host and have an unknown history. Fine-grained white mica from both layers were selected for K-Ar dating.

The low-T mylonites are related to Pfaffenchopf deformation, which is very localized (Fig. 2). Two low-T mylonites are investigated, which differ slightly in their mineralogy (Figs. 1, 2, 3 and Table 1). In addition, four fault gouges are selected for analysis.

These fault gouges are subdivided into two from the Handegg area (overprinting ductile Handegg shear zones) and two from the Innertkirchen area (close to low-T-mylonites; Fig. 2a).

4 Methods

4.1 Sample preparation

The mylonite samples are crushed by Selfrag mineral liberation (Zwingmann et al. in review; Sperner et al., 2014; Giese et al., 2010). Gouge samples consisted of >0.5 kg cohesionless material providing fine clay like material, sand fraction and mineral aggregates. The fine clay material is associated with the gouge formation, and no artificial mineral liberation was required. Both artificially liberated mineral samples and cohesionless gouges samples where then sieved to obtain particles < 500 µm. Grain size fractions of 6-10 µm and 10-20 µm were separated by gravity settling using Stokes law (Atterberg settling tubes). In addition, grain size fractions <0.8, 0.8-2, 2-5, 2-6 µm were obtained using a swing rotor centrifuge. Large grain sizes (>60 µm) were handpicked (Table 2).

4.2 Microstructures, element mapping, mineral chemistry and thermobarometry

Thin sections were cut from larger rock fragments and aggregates; these sections were then studied with the optical light microscope to confirm the host rock composition. Petrographic investigations involved light and electron microscopy. Scanning electron microscopy was performed on a ZEISS EVO50 using backscatter and charge contrast images. Electron microprobe analyses (EMP) were performed using a JEOL superprobe JXA8200 instrument at the Institute of Geological Sciences of the University of Bern. The analysis of sheet silicates was conducted at 15 kV and 5-8 nA, using natural and synthetic standards for major elements (SiO_2, Al_2O_3, FeO, MnO, MgO, CaO, Na_2O, K_2O). X-ray element mapping was conducted using wavelength dispersive spectrometers at 15 kV and 100 nA with dwell time ranging between 100 and 200 ms. The compositional maps were standardized using a series of spot analyses measured on the same area. The data were reduced using the program XMapTools 2.2.3 (Lanari et al., 2014a). The primary data (X-ray counts uncorrected for background) were standardized after the classification using the automatic function provided in XMapTools. Structural formulae calculations (on a basis of 11 and 14 atoms of oxygen for K-white mica and chlorite, respectively) were

applied to all the pixels based on the atom site repartition models used in the thermodynamic models (see below). The pixel compositions of K-white mica and chlorite are reported as element maps (in atoms per formulas unit) to highlight the relationships between the compositional zoning and the microstructures (see Scheffer et al. 2016).

The chemical subdivisions into distinct groups are based on differences in mineral chemistry related to substitutions. The compositional variability of chlorite in the system SiO_2-Al_2O_3-FeO-MgO is described by three main substitutions (i) FM: Fe^{2+}= Mg^{2+}, (ii) Tschermak: Si+(Mg^{2+}, Fe^{2+}) = 2Al and (iii) di-trioctahedral: (Mg^{2+},Fe^{2+})$_3$= 2Al (Cathelineau and Nieva, 1985; Lanari et al., 2014c), whereas additional substitutions take place in the ferric system (Trincal and Lanari, 2016; Vidal et al. 2016). The compositional variability of K-white mica is modeled in the system SiO_2-Al_2O_3-FeO-MgO-Na_2O-K_2O, based on the definitions of Dubacq et al. (2010), using the following end-members: muscovite ($Si_3Al_3\square_1K_1O_{10}(OH)_2$); Fe/Mg-celadonite ($Si_4Al_1$ $(Fe/Mg)_1$ $\square_1K_1$ O_{10} $(OH)_2$); phlogopite ($Si_3Al_3Mg_1K_1O_{10}(OH)_2$); pyrophyllite ($Si_4Al_2\square_2O_{10}(OH)_2$); and paragonite ($Si_3Al_3\square_1Na_1O_{10}(OH)_2$). The main exchanges led to vacancies in the A-site due to K-free components and to changes in Al(tot) related to celadonite and pyrophyllite exchange reactions (e.g., Parra et al., 2001; Dubacq et al., 2010). This led to the main exchange vectors: paragonite-muscovite exchange [KNa_{-1}], tschermak: Si+(Mg^{2+}, Fe^{2+}) = 2Al and pyrophyllite-vector [$(K,Na)_{-1}\square_1$]. P-T estimates of high variance assemblages are generally achieved with the technique of multi-equilibrium (Vidal and Parra, 2000; Vidal et al. 2006). Several calibrations have been developed and the most recent of them are used in this study: Chlorite + Quartz + Water (Lanari et al. 2014) and Phengite + Quartz + Water (Dubacq et al. 2011). A comprehensive description of this technique based on the progressive hydration of the vacancies along a P-T divarient equilibrium curve is provided together with application examples in Lanari et al. (2012). Computations were achieved using the in-house program ChlMicaEqui (Lanari, 2012).

4.3 Clay minerals

Oriented sample separates were achieved by settling of the grain size fractions onto silica wafers. Diffractograms were made for all grain size fraction using XPERT PRO PANalytical diffractometer with CuKα radiation and 40 kV/40 mA. Samples were scanned over the range 2θ= 4 - 60° at 0.0167° 2θ/s. Additional measurements of the smallest grain size fraction for air dried, glycolated and heat treated slides were performed in order to distinguish between smectite, kaolinite and chlorite (Moore and

Reynolds, 1989) for which sample separates were sedimented onto glass slides. The diffractograms were obtained using a Philips PW 1710 diffractometer with samples scanned over the range of 2θ= 2 - 40° at 0.02° 2θ/s (Table 2). In selected gouges, the diffraction pattern was Rietveld-refined with TOPAS-Academic V6 (Coelho, 2012). For refinement, March-Dollase preferred orientation parameters of both illite structures (1M and 2M) were constrained to the same value (0.565(3)).

4.4 K-Ar dating

A standard method, described elsewhere (Dalrymple and Lanphere, 1969), was used for K-Ar dating. The potassium content was determined by atomic absorption. Duplicate K determination on several samples and standards resulted in a pooled error better than 2.0 %. A procedure comparable to the one used by (Bonhomme et al., 1975) was used for Argon isotopic determinations. Several hours of pre-heating under vacuum at 80°C served to reduce the amount of Argon adsorbed onto the mineral surface during sample preparation.

Argon was extracted from the separated mineral fractions by fusing samples within a vacuum line serviced by an online ^{38}Ar spike pipette. An on-line VG3600 mass-spectrometer was used to measure the spiked Ar via Faraday cup. The ^{38}Ar spike was calibrated against biotite GA1550 (McDougall and Harrison, 1999). After fusion, the released gases underwent a two-stage purification procedure via CuO and Ti getters. A systematic determination of blanks for the extraction line and mass spectrometer was carried out. The mass discrimination factor was determined by airshots. Argon analyses required around 20 mg of sample material. During the course of this study, the international standards GLO (Odin et al., 1982) and HD-B1 (Hess and Lippolt, 1994) were measured several times (n=5). The error for Ar analyses is below 1.00 % (Table 2) and the $^{40}Ar/^{36}Ar$ value for airshots averaged 295.05 ± 0.35 (n = 5, Table 3). ^{40}K abundance and decay constants suggested by Steiger and Jager (1977) allowed for K-Ar age calculation. Errors are listed within 2 sigma.

5 Results

5.1 Mylonites

Sample GRS05 contains fine-grained deformed layers. The latter consist of biotite, white mica, quartz, epidote and minor amounts of feldspar (Figs. 3, 4; Table 4). The

278 fine-grained biotite and white mica (4-50 µm) are related to syn-deformational
279 (re)crystallization. The mylonite contains large mica flakes (100-400 µm), with
280 unknown pre-deformation history and newly formed grains related to mylonitization
281 (down to 3 µm).
282 The EMP-analyses of white mica from sample GRS06 show one composition (Fig. 5;
283 Table 5). This composition is consistent with the white mica in mylonitic bands as
284 well as in the surrounded schistose material. Sample GRS05 shows only limited
285 spread in white mica composition with an average SiO_2 content of 47 wt%, this is
286 notably independent of grain size. The Na_2O content is below 0.1 wt%. For
287 comparison the white mica from sample KAW2214 is measured (Figs. 1 and 5; Table
288 1). The biotite bearing mylonites contain white mica with low Na content, but a slight
289 temperature effect from north to south can be inferred (Fig. 5). These data overlap
290 with white mica compositions from the literature further south (Challandes et al.,
291 2009; Goncalves et al., 2012). The ductile deformed samples show a consistent K-Ar
292 age range, which is spread between 11.8 ± 0.2 and 13.6 ± 0.3 Ma (Table 6; Fig. 6).
293 The different grain size fractions give similar ages inside one sample and no
294 relationship between grain size and age can be observed.
295

296 ## 5.2 Low-temperature mylonites

297 ### 5.2.1 Microstructures

298 Two investigated samples deformed at the frictional-viscous transition (see Table 1).
299 Deformation conditions are characterized by brittle deformation of feldspar and
300 quartz. Quartz grains occasionally show bulging recrystallization. The overall
301 deformation has been classified as ductile, which is caused in the deformation-
302 behavior of the sheet silicates. However, also large white micas and chlorite (100 -
303 400 µm) are observed (Fig. 7b, c). They show bending into strain localization planes
304 (Fig. 7). These planes are characterized by both fine-grained phase mixtures and
305 local chlorite/mica intergrowth. In addition local hydrothermal veins developed, which
306 are related to brittle deformation (see the base of the optical microphotograph in Fig.
307 8a). The micas dominate the deformation. The white micas are designated into the
308 following microstructural groups (Table 7):
309 *mi1*: Several large grains occur as relics in the mylonites. This microstructure is
310 more frequent in sample Gr66 as in sample Ga14-2 (Figs. 7 and 8).
311 *mi2*: This microstructure is characterized by small grains in the direct vicinity of
312 larger mica grains Fig. 7). The process of dynamic recrystallization could be

responsible of this microstructure type. However, the single slip-plane of mica makes dynamic recrystallization problematic (e.g., Shea and Kronenberg, 1992). Alternatively, fracturing in combination with preexisting stacking faults can produce such a microstructure. This indicates fracturing inside the preexisting grains and their shearing along the (001) plane. The grain size of identified new grains is in the range of 2-5 µm.

mi3: These micas grew while isolated in the recrystallized quartz or quartz/feldspar matrix by solution/precipitation (Fig. 7). The grain size of this group is relatively constant (2-5 µm; Table 7). This microstructure is comparable with the microstructure in the intermediate temperature mylonites.

mi4: Mica pseudomorphs grown at the expense of precursor minerals (Figs. 7 and 8). These pseudomorphs are occasionally dominated by white mica, but also chlorite-white mica mixtures occur. In addition, fine-grained alteration of feldspars is observed, producing muscovite and, locally, epidote. The chemical composition of such white micas may have been controlled by the local bulk composition during the reaction that probably differs from the local bulk composition of the matrix (see details in section 5.2.3).

mi5: This group of mica can only be identified in combination of microstructure and mineral-chemistry data. This process developed patches with variable chemistry (Figs. 7, 8). Such changes of chemistry without obvious change in microstructure requires a process described as pseudomorphic replacement (Putnis, 2002; Airaghi et al. 2017). Such replacement structures can be inferred in single grains as well as in grain aggregates (Fig. 7).

5.2.2 Mineral chemistry and P/T data

The mineral-chemistry of the white mica is divided into the following compositional groups: (A) low Al (high Si) -contents; (B) high Al (low Si) at similar Na contents; and (C) high Al and high Na contents (Fig. 5). The compositional group A is characterized by high Si content (Si ~3.3 apfu (=atoms per formula unit)), low Al content (Al ~1.5 apfu), high Mg content (Mg ~0.23 apfu) and low Na content (Fig. 5). This group is systematically associated with newly formed chlorite and is interpreted as newly formed grains. These newly formed white mica indicate temperatures in the range of ~300°C (assuming a pressure of 3-4 kbar and a_{H2O}=1; Fig. 9). This result is consistent with independent temperature estimates derived from chlorite compositions associated with such white micas (Fig. 9). In sample Ga14-2, rare and isolated calcite grains indicate possible lower water activity (if calcite is reacting at

the same time as the white mica). A lower a_{H2O} would slightly decreases the resulting temperature for the white mica by 20-30°C (Fig. 9). The group-C micas are related to alteration of group-A mica and new growth in hydrothermal pockets. These micas are characterized by high, but variable Na-contents. Some of the high Na contents are associated with decreasing interlayer content (increase of the pyrophyllite component, Fig. 10b; see section 6.2).

5.2.3 Ar-data

Six fractions from two samples are measured, which yield apparent K-Ar ages between 19.9 ± 0.4 Ma to 39.8 ± 0.8 Ma (Tables 3 and 6; Fig. 6). The coarse grains are systematically older than the fine fraction (Table 6). However, the absolute values of ages at given grain size differ between the two samples. The fine grain size fraction (<0.8µm) of sample Ga14-2 is apparently older than the fraction 2-6 µm in Gr66 (Table 6). However, the selected large grains have apparent ages in the same range (37 and 40 Ma; Table 6; Fig. 6), which is significantly lower than literature data from undeformed samples in the area (compare white mica age of KAW2385 versus Gr66/Ga14-2; Table 1).

5.3 Fault-gouges

Gouges from the southern- and the northern areas are investigated (Figs. 1 and 2; Table 1). Sample He12 from the southern area is collected from a several cm wide fault gouge overprinting a ductile shear zone (Table 1). The symmetric shear zone shows an increase of deformation from weakly deformed host rock over schistose granite to mylonite. Orientation of the fault plane is steeply south dipping. The fault gouge in the centre with a width of several cm consists of fine clay material, where a lineation measured on the clay surface is subhorizontal. This lineation can easily be swiped away by hand and has been established as a slickenside lineation (Doblas, 1998). This type of slickenside may develop by the ploughing of harder minerals (i.e. quartz) into the clay matrix during block movements. The gouge is cohesionless and no defragmentation was required prior to clay separation (Table 2). The second sample from the southern area (sample He15; Table 1) is collected from a 10 cm wide fault zone. The shear zone is asymmetric and ranges from weakly schistose granitoid in the south toward mylonite (Fig. 2). The orientation of the fault surface is steeply dipping toward the south. The slickenside lineation on the clay surface is

subhorizontal. Also here, collected material consists of fine clay material with a contribution of larger fragments.

The investigated fault gouges of the northern area are cross cutting all other structures (Figs. 3 and 4). They are both NE-SW to NEE-SWW striking and steeply dipping toward the south. A lineation plunging down dip was visible on the gouge surface of sample Ik1206, whereas the lineation on the clay surface of Ik1206 is subhorizontal in orientation. These fault gouges are about 10 cm wide. All fault gouges consisted of fine-grained matrix material and fragments. The fragments are relics inside the gouge, which show a composition/microstructure similar to the proximal mylonites. The mylonitic microstructure is preserved in these fragments confirming the overprint of a former a ductile shear zone by the fault gouge. The two northern samples differ in their microstructures from the incorporated clasts. Sample Ik1206 shows in all inspected fragments highly mylonitic structures with fine-grained mica aggregates as described before for the low T-mylonites of the area (Fig. 11). The mineral-chemistry of these micas is comparable with those of adjacent mylonites (Fig. 11). In contrast, blocky quartz and large mica grains characterize sample Ik1202 (Fig. 11). The gouge material itself contains smectite, chlorite and illite/white mica and kaolinite (Table 4). The smectite fraction is the highest in the smallest grain size (< 0.8µm). Furthermore, the proportion of smectite increases with the decreasing grain size. This indicates that smectite is newly formed in the small grain size fraction (Table 4). This is better evolved in the southern than in the northern samples (Table 4). illite, quartz and chlorite/kaolinite were identified in the fine-grained fractions. Rietveld refinements demonstrate the occurrence of both 1M and 2M structures (see section 4.3). XRD-data results point to a ~15% fraction of M1-structures (M2-illite: ~77%, Quartz: ~8%, Kaolinite/Chlorite: ~1%; Fig. 12). As already mentioned for smectite (Table 5), the amount of newly formed low-grade clay minerals is insufficient to date these phases (see below; the potential to unravel the difference in age between the inherited minerals and newly formed minerals, which is short in the investigated examples).

The fault gouges of the southern area (sample He12 and He15) show an age spread between 11.3 ± 0.3 -14.4 ± 0.4 Ma with the exception of the smallest grain size of sample He15 (Fig. 6). The latter data can be excluded, because of the low K-content (Table 6). The fault gouges of the northern area differ between the two sample sites, but in both samples no relationship between grain size and age can be inferred. Sample Ik1202 show ages between 33.0 ± 0.7 and 36.8 ± 0.7 Ma, whereas sample Ik1206 gives results of apparent ages between 18.9 ± 0.4 and 21.1 ± 0.4 Ma (Table

6). The different age groups of these two samples correspond well with completely different microstructures of the clasts in these samples (Fig. 11).

6 Discussion

The results for mylonites, low-T mylonites and cohesionless fault gouges illustrate changes in the size of equilibrium-volumes, which is related to temperature and deformation conditions. In the following, the different tectonites are first addressed separately and then compared and integrated in a general model (see section 7).

6.1 Hydrothermal veins inside mylonites

Sample GRS06 shows multiple veins consisting of mylonitized pure quartz and white-mica quartz aggregates (Fig. 4). Neocrystallized white mica in the deformed vein with a grain size of 2-6 µm is compared with larger fractions, up to handpicked mineral sizes. The K-Ar ages for the different grain size fractions are, within uncertainty, identical (Fig. 6). In principal, the obtained age could be related to (i) diffusive re-equilibration, (ii) net-transfer reactions and recrystallization, or (iii) inheritance of older deformation / metamorphic phases (e.g., Villa, 1998; Allaz et al., 2011; Villa et al., 2014). Dodson-type cooling ages are based on diffusional length scale and should relate to grain size (Dodson, 1973). This is not the case in the high temperature mylonite samples, and the meaning of the ages as diffusive re-equilibration or “cooling age” (i) can therefore be dismissed (Fig. 6). More recent studies proposed fluid circulation and recrystallization as important processes in closing the isotopic system (Villa and Hanchar, 2013; Allaz et al., 2011; Villa, 1998). Our structural data indicates that the newly formed white mica is the result of recrystallization (section 4). Any inheritance (iii) of an older deformation phase or crystallization would be noticeable, especially in the age of larger grains (Villa et al., 2014), which is again not the case in these samples.

The obvious deformational induced recrystallization of the fine fraction and the, within error, similar ages of the large grains indicates contemporaneous deformation and hydrothermal veining (ii). The age of larger handpicked grains may reflect a hydrothermal event with subsequent deformation. This excludes mixed ages for the recrystallized micas in these mylonites. The resulting age in this sample is therefore linked to the hydrothermal activity during shearing of the mylonite.

6.2 Mineral reactions, mica petrology and P-T data in low-T mylonites

The low-T mylonites contain different microstructures, some of them are connected to precursor minerals (e.g., *mi4*: pseudomorphs, *mi5*: pseudomorphic replacement, Table 7, section 5.2). In these two example microstructures, a net-transfer reaction is necessary. Two important groups of reactions are inferred from microstructures and inherited minerals:

garnet + K_2O + H_2O => white mica + chlorite + CaO (1)

biotite + H_2O => white mica + chlorite (2)

Replacement structures and re- or neocrystallization require reaction of the type:

white $mica_1$ => white $mica_2$ (3)

In contrast to reaction (1) and (2), reaction (3) does not necessary require the nucleation of new crystals and can be accommodated by diffusion, dissolution / reprecipitation and mineral replacement (Putnis, 2002; Putnis and Austrheim, 2013; Fig. 8). Independent of the inferred reaction, the product compositions are different. It is important to highlight here that the compositions of the newly formed white micas define characteristic compositional groups that are observed at the thin section scale suggesting the achievement of local equilibrium. The local equilibrium is not only controlled by the local solid phases, but also by the fluid. The occurrences of limited mica-compositions indicate an important role of the circulating fluid for such local equilibriums.

The combination of microstructures and mineral-chemistry data document mainly a change from chemical composition of group A to group C. This change in mineral-chemistry requires an exchange vector of the type $K_{-1}Al_{-1}Si$, which can be written as an exchange reaction:

$mica_A$ => 1+x $mica_C$ + x Al_2O_3 (4a)

or:

$mica_A$ + SiO_2 => $mica_C$ + K_2O (4b)

This suggests not only a change in the Si/Al ratio, but also an increase in vacancies (pyrophyllite component). However, the detected increase in vacancies is systematically small and the major change is related to $K_{-1}Na$ exchange (Fig. 10). The change in K/Na ratio in the white mica requires either transport of these elements in a fluid and/or a reaction involving K/Na minerals (i.e. feldspars).

The change in composition between groups A and C includes possible paragonite-, celedonite- and pyrophyllite exchange vectors (e.g., Livi et al., 1997; Agard et al., 2001; Dubacq et al., 2010). The K- and Na-data mainly shows a paragonite exchange (NaK_{-1}; Fig. 10a). An increased paragonite component in white mica coexisting with paragonite is related to a temperature increase, which can be derived

490 from the shape of the muscovite-paragonite solvus (e.g., Keller et al. 2005). If
491 paragonite is not present, the absolute Na-concentrations depend on the coexisting
492 phases and fluid, i.e. the composition of the equilibrium volumes (= reactive bulk
493 composition, see Lanari and Engi 2017). Large variations of Na-content and Si/Al
494 ratios occur in sample Gr66, where the micas with higher Na contents (group C)
495 clearly formed along the retrograde path, i.e. at lower temperature than the Na-poor
496 K-white micas.
497

498 ### 6.3 Relationship between microstructure, mica composition and Ar-data in
499 low-T mylonites

500 The different mica compositions occur at different microstructural positions in the
501 different samples (Fig. 13). For example, the high-Na mica in sample Ga14-2 is
502 observed in the highly deformed domains (Fig. 8f), in the grains of the upper section
503 of Figure 8a, and around the garnet porphyroblast (see Fig. 8a). But this group also
504 occurs as small grains in the matrix (microstructure “mi3”, see Fig. 8), where mineral
505 composition A dominates. In this case, the link between microstructural position and
506 composition is not unique, but again only a limited number of compositional groups
507 can be defined (Fig. 5). For example composition “C” occurs in replacement
508 structures and at locations of recrystallization (Fig. 13). Moreover, the composition of
509 white mica seems to be independent of the local mineral assemblage. The
510 occurrence of the same white mica composition in different microstructures indicates
511 equilibrium with a fluid. It is important to note here that a large part of the rock is not
512 reacting during the formation of the new white mica generation. This process can
513 explain the formation of white mica with the same composition in domains with
514 different unreactive assemblages. The equilibrium volume depends on the type and
515 size of the fluid-mineral exchange volume. In our sample the changes from one to
516 another compositional group suggest change in the P-T-(X) conditions. However, the
517 differing equilibration volumes depend on microstructure and the related equilibration
518 processes between fluid and deforming mica (e.g., Putnis, 2002; Lanari et al., 2014b;
519 Airaghi et al. 2017).
520 Changing P-T conditions along a given P-T-D-t path involve tectonic processes. This
521 prerequisite has been intensively invoked at other locations with the combination of
522 petrological and Ar investigations (McAleer et al. 2017; Angiboust et al., 2014; Lanari
523 et al. 2014b; Sanchez et al., 2011; Augier et al., 2005; Agard et al., 2002; Cosca et
524 al., 1998; Markley et al. 1998). In in-situ laser ablation studies for instance, the
525 microstructure of micas were successfully linked to Ar isotope ages (e.g., Agard et al.

526 2002, Schneider et al., 2013; Mulch et al., 2002). Some studies extracted Ar from
527 carefully selected areas of multiple grains (e.g., Agard et al., 2002), whereas other
528 studies select large single grains (e.g., Mulch et al., 2002). Several issues in such
529 datasets can be overlooked without direct petrological control (see this study, Kellett
530 et al. 2016). From a theoretical point of view, only the newly formed (and isotopically
531 reset) grains should be analyzed and they remain small in the temperature range of
532 interest (e.g., Gueydan et al. 2003). The complexity of white mica major element
533 chemical zoning has been highlighted in several studies and the re-equilibration
534 commonly involves dissolution-precipitation processes instead of new growth
535 (Scheffer et al. 2016; Airaghi et al. 2017). To obtain isotopic analyses of the newly
536 grown crystals only, one can apply analyses for different grain sizes and select the
537 smallest fraction. Therefore, grain size sensitive analysis may be the optimal tool to
538 unravel such processes with K-Ar techniques. This method has been successfully
539 applied to fault gouges (e.g., Zwingmann et al. 2004; Zwingmann, 2014 and
540 references therein). Conventional K-Ar dating was used instead of $^{39}Ar/^{40}Ar$ dating to
541 avoid ^{39}Ar recoil artifacts or encapsulation corrections (Zwingmann, 2014).
542 In the investigated example, recrystallization and fracturing of mica produces
543 isolated, ultrafine grains (Figs. 7, 8, 13, 14 and Table 7). The selection of these fine
544 grains may relate to the dominant deformation stage of the sample. However, as
545 seen in the mineral chemistry also relic chemistry can be retained in small grains, if
546 fracturing is an important process (Figs. 7, 8 and Table 7). Vice-versa, large grains
547 can change their chemistry by replacement processes without changing the grain
548 size (Putnis, 2002; Airaghi et al., 2017). This allows perturbation of isotope
549 information in different grain size fractions, which corresponds with an apparent
550 partial resetting of the large grains in comparison to literature gneiss data (Table 1).
551 In addition, relics of fractured grains are responsible in the fine fraction for apparent
552 ages being too old (Fig. 14). Neither the grain size nor the position of certain micas
553 correlates with chemical groups of micas.
554

555 ### 6.4 Isotope data in gouges
556 Dating of gouge formation can be successful if K-bearing phases are neoformed
557 (e.g., Zwingmann, 2014; Bense et al., 2014; Viola et al., 2013; Clauer, 2013; Pleuger
558 et al., 2012; Solum et al., 2005; Zwingmann and Mancktelow, 2004; Zwingmann et
559 al., 2004, 2010; van der Pluijm et al., 2001; Torgersen et al., 2015; Mancktelow et al.
560 2015; Viola et al., 2016). In this context, knowledge of the amount of newly formed

illite versus inherited detrital muscovite is important to assess the significance of "mixed" ages. In the investigated gouges, the following points can be highlighted:

(1) Gouge samples show no systematic trend between grain size and age (Fig. 6).
(2) Grain size reduction of the mylonite hosting K-bearing phases resulted in clay size particles during the gouge formation (no crushing were applied).
(3) Relative high smectite fractions in the fine fractions indicate formation at very-low temperature.
(4) Decreasing K-content with increasing smectite content (sample He12) suggests K-loss via low temperature fluids.
(5) Owing to overprinting/reactivation of inherited deformation structures, detritus in the gouges is more likely sourced from precursory mylonites.

In this view, the gouge hosts similar processes as the multistage samples. However, due to missing newly formed K-phases during gouge formation, no age information for the brittle deformation can be gained. The K-bearing relics in the gouges can be seen as chemically unaltered fragmented minerals originating from the precursor mylonites. The K-Ar ages of the gouges are therefore similar to the surrounded mylonites, which is the 12-14 Ma isotope ages in the southern area (sample He12 and He15) and the apparent 19 Ma data in the Innertkirchen area (Table 6). These ages are most likely inherited from surrounded material, indicating a mechanical grain size reduction processes during brittle deformation (fracturing of sheet silicates). Furthermore, the clay sometimes used mineralogy (e.g., M1-illite; Solum et al. 2005, 2010, Fitz-Diaz and van der Pluijm 2013) does not correlate with apparent ages gained from K-Ar dating in our example (Table 5 and 6). Our results, as data in other studies, indicate that K-Ar dating should be considered in combination with microstructural and chemical analysis (e.g., Mancktelow et al. 2015).

6.5 Geological implications for the Aar-massif

The presented Ar-data in the mylonites record ductile deformation in the central part of the Aar-massif (see Tables 2 and 6). The obtained new data are similar and overlap with results further south (Fig. 15; Rolland et al., 2009; Challandes et al., 2008; Rossi and Rolland 2014; Table 1). Considering the uncertainty, the deformation age of the investigated Handegg- and the strike-slip shear zone in the center of the massif are overlapping. This model fits well with the suggested transition of the two phases at ~12 Ma as documented by synkinematic open cleft monazite in the Oberaar area further south (Bergemann et al., 2017). Owing to

aforementioned structo-chemical interactions, and the lack of an adequate spatial analysis technique for fine-grained minerals, the K-Ar data in the northern area provides no constraints on the timing of the Pfaffenchopf- and Gadmen- deformation phases. However, all data in high strain tectonites differ from literature data, which is derived from less deformed host rocks (Table 1; Dempster, 1986). Therefore, only the detail knowledge of overprinting relationships and geological evolution allow the interpretation of such fault-related data.

7 Summary of white mica evolution

Comparing different deformation processes in granitoid to gneissic basement units, both the mechanical role of deformation and the abundance of sheet silicates increase with decreasing temperature. With decreasing metamorphic grade, microstructures of polymineralic assemblages indicate an evolution from viscous granular flow over solution/precipitation to fracturing, finally resulting in frictional granular flow of sheet-silicate-rich fault gouges. This occurs over a range of varying mineral stabilities, from biotite bearing mylonites over low-temperature mylonites containing white mica/chlorite down to smectite-bearing cohesionless gouges (Fig. 14). Particularly the deformation behavior of white mica is linked to mineral reactions, which influence both the chemical adaptation processes and the grain sizes. At high temperatures, the micas are chemically completely equilibrated/reset during multiphase viscous granular flow by processes like dissolution, mass transfer and precipitation within the entire aggregate. This resetting allows robust K-Ar dating of such rock types by multigrain analysis. In the low temperature mylonites, fracturing becomes increasingly important, and local mineral equilibria dominates (Fig. 14). The combined variable efficiency of different chemical exchange processes generates white mica in different grain sizes and compositions. At these conditions, kinetics and the resulting local mineral-chemistry depends strongly on the intergranular transport, reactive bulk composition and the solubility of elements in fluids. The reactivity of white mica is related to the exchange rate with a fluid. This exchange (or equilibration) rate depends on grain size and the overall intergranular connectivity, but can generally be said to decreasing with temperature. Although fluid accessibility is enhanced in the fault gouges and chemical precipitation processes still occur, the latter being demonstrated by the formation of smectite, temperatures and K-activity are too low for white mica/illite equilibrium on the retrograde path in our samples.

631 Identifying equilibrated mica at the sample scale requires the combination of micro-
632 structural data and mineral chemistry. The increasing role of fracturing in low
633 temperature mylonites and decreasing exchange volumes with fluids allows for the
634 preservation of different micas along the T-D path of the investigated mylonites. This
635 preservation in combination and the knowledge of local equilibrium is an important
636 aspect for selecting micas for geochronology but can also be used as a chemical
637 proxy for the detection of local equilibria/disequilibria.
638
639
640 **Acknowledgements**

641 We are grateful to an anonymous reviewer and Juan Jimenez-Millan for their constructive reviews and
642 to P. Agard for efficient editorial handling and additional suggestions that greatly improved the clarity
643 of this work. We thank James Gilgannon for careful English corrections. We would like to thank the
644 following people and institutions for their support in the overall project: Kraftwerk Oberhasli AG.,
645 Christine Lemp, Martin Fisch, Urs Eggenberger, Igor Villa, and Reto Wagner. Andrew Todd, CSIRO is
646 thanked for technical assistance. Financial support by SNF (project 200021132196) is greatly
647 acknowledged.
648
649

650 **References:**

651 Abrecht, J., 1994. Geologic units of the Aar massif and their pre-Alpine rock associations, a critical
652 review: The pre-Alpine crustal evolution of the Aar-, Gotthard-and Tavetsch massifs.
653 Schweiz. Mineral. Petrogr. Mitteil. 74, 5-27.

654 Agard, P., Vidal, O., Goffé, B., 2001. Interlayer and Si content of phengite in HP–LT carpholite-
655 bearing metapelites. J. metamorphic Geol., 19, 479–495

656 Agard, P., Monie, P., Jolivet, L. & Goffe, B., 2002. Exhumation of the Schistes Lustre´s complex: in
657 situ laser probe 40Ar/39Ar constraints and implications for the Western Alps. Journal of
658 Metamorphic Geology, 20, 599–618.

659 Agard, P., Searle, M. P., Alsop, G.I., Dubacq, B., 2010. Crustal stacking and expulsion tectonics during
660 continental subduction: P-T deformation constraints from Oman. Tectonics 29, TC5018, 1-19.

661 Airaghi, L., Lanari, P., de Sigoyer, J., Guillot, S., 2017. Microstructural vs compositional preservation
662 and idiomorphic replacement of muscovite in deformed metapelites from the Longmen Shan
663 (Sichuan, China). Lithos, 282-283, 262-280.

664 Allaz, J., Engi, M., Berger, A., Villa, I., 2011. The effects of retrograde reactions and of diffusion on
665 40Ar–39Ar ages of micas. Journal of Petrology 52, 691-716.

666 Augier, R., Agard, P., Monié, P., Jolivet, L., Robin, C., & Booth-Rea, G., 2005. Exhumation, doming
667 and slab retreat in the Betic Cordillera (SE Spain): in situ40Ar/39Ar ages and P–T–d–t paths
668 for the Nevado-Filabride complex. Journal of Metamorphic Geology, 23, 357–381.
669 doi:10.1111/j.1525-1314.2005.00581.x

670 Bambauer, H.U., Bernotat, W., Breit, U., Kroll, H., 2005. Perthitic alkali feldspar as indicator mineral
671 in the Central Swiss Alps. Dip and extension of the surface of the microcline/sanidine
672 transition isograd. European Journal of Mineralogy 17, 69-80.

673 Bense, F.A., Wemmer, K., Löbens, S., Siegesmund, S., 2014. Fault gouge analyses, K–Ar illite dating,
674 clay mineralogy and tectonic significance—a study from the Sierras Pampeanas, Argentina
675 International Journal of Earth Sciences 103, 189-218.

676 Bergemann, C., Gnos, E., Berger, A., Whitehouse, M., Mullis, J., Wehrens, P., Janots, E., 2017. Th-Pb
677 ion probe dating of zoned hydrothermal monazite and its implications for repeated shear zone
678 activity: An example from the Central Alps, Switzerland. Tectonics, 36,
679 doi:10.1002/2016TC004407

680 Bonhomme, M., Thuizat, R., Pinault, Y., Clauer, N., Wendling, R., Winkler, R., 1975. Méthode de
681 datation potassium-argon, appareillage et technique, Institut Géologie, Strasbourg Notes
682 Techniques 3, 35

683 Bousquet R. et al. , 2012. Metamorphic framework of the Alps. Map of CCGM/CCMW,

684 Cantarero, I., Lanari, P., Vidal, O., Alias, G., Travé, A., Baqués, V, 2014. Long-term fluid circulation
685 in extensional faults in the central Catalan Coastal Ranges, P-T constraints from neoformed
686 chlorite and K-white mica. International Journal of Earth Sciences. 103, 165-188.

687 Carlson, W. D. 2010. Dependence of reaction kinetics on H_2O activity as inferred from rates of
688 intergranular diffusion of aluminium. J. metamorphic Geol., 28, 735-752.

689 Cathelineau, M., Nieva, D., 1985. A chlorite solid solution geothermometer the LosAzufres, Mexico.
690 geothermal system. Contrib. Mineral. Petrol. 91, 235–244.

691 Challandes, N., Marquer, D., Villa, I., 2008. P-T-t modelling, fluid circulation, and 39Ar- 40Ar and
692 Rb-Sr mica ages in the Aar Massif shear zones, Swiss Alps.. Swiss Journal of Geosciences
693 101, 269-288.

694 Choukroune, P., Gapais, D., 1983. Strain pattern in the Aar Granite, Central Alps., Orthogneiss
695 developed by bulk inhomogeneous flattening Journal of Structural Geology 5, 411-418

696 Clauer, N., 2013. The K-Ar and 40 Ar/39 Ar methods revisited for dating fine-grained K-bearing clay
697 minerals. Chemical Geology 354, 163-185.

698 Coelho, A. A., 2012. TOPAS Academic. Version 5. Coelho Software, Brisbane, Australia.

699 Cosca, M., Arculus, R., Pearce, J., & Mitchell, J., 1998. 40Ar/ 39Ar and K–Ar geochronological age
700 constraints for the inception and early evolution of the Izu–Bonin – Mariana arc system.
701 Island Arc, 7(3), 579–595. doi:10.1111/j.1440-1738.1998.00211.x

702 Dalrymple, G. B., and Lanphere, M. A., 1969. Potassium-Argon Dating. San Francisco: W.H.
703 Freeman. 258 p.

704 Dempster, T., 1986. Isotope systematics in minerals, biotite rejuvenation and exchange during Alpine
705 metamorphism. Earth and Planetary Science Letters 78, 355-367.

706 Derkowski, A,. Szczerba, M., Środoń, J., Banaś, M., 2014. Radiogenic Ar retention in residual silica
707 from acid-treated micas. Geochimica et Cosmochimica Acta, 128, 236-248.

708 Doblas, M., 1998. Slickenside kinematic indicators Tectonophysics 295, 187-197.

709 Dubacq, B., Vidal, O., Andrade, V., 2010. Dehydration of dioctahedral aluminousphyllosilicates,
710 thermodynamic modeling and implications forthermobarometric estimates. Contrib. Mineral.
711 Petrol. 159, 159–174.

712 Dubacq, B., Vidal, O., Lewin, E., 2011. Atomistic investigation of the pyrophyllitic substitution and
713 implications on clay stability. American Mineralogist, 96, 241-249.

714 Faulkner, D.R., Jackson, C.A.L., Lunn, R.J., Schlische, R.W., Shipton, Z.K., Wibberley, C.A.J.,
715 Withjack, M.O., 2010. A review of recent developments concerning the structure, mechanics
716 and fluid flow properties of fault zones. Journal of Structural Geology, 32, 1557-1575.

717 Fitz-Diaz, E., van der Pluijm, B., 2013. Fold dating: A new Ar/Ar illite dating application to constrain
718 the age of deformation in shallow crustal rocks. Journal of Structural Geology 54, 174-179

719 Fourcade, S., Marquer, D. & Javoy, M., 1989. $^{18}O/^{16}O$ variations and fluid circulation in a deep shear
720 zone – the case of the alpine ultramylonites from the Aar-massif Central-Alps, Switzerland.
721 Chemical Geology, 77, 119–131.

722 Frey, M., Bucher, K., Frank, E., Mullis, J., 1980. Alpine metamorphism along the geotraverse Basel-
723 Chiasso, a review. Eclogae Geologicae Helvetiae 73, 527-546.

724 Frey, M., Ferreiro Mählmann, R., 1999. Alpine metamorphism of the Central Alps Schweiz. Min. Petr.
725 Mitt. 79, 135-154.

726 Giese, J., Seward, D., Stuart, F. M., Wüthrich, E., Gnos, E., Kurz, D., Eggenberger, U. and Schreurs,
727 G. 2010. Electrodynamic disaggregation, does it affect apatite fission-track and, U–Th./He
728 analyses? Geostandards and Geoanalytical Research, 34, 39-48.

729 Goncalves, P., Oliot, E., Marquer, D., Connolly, J.A.D., 2012. Role of chemical processes on shear
730 zone formation, an example from the Grimsel metagranodiorite, Aar massif, Central Alps. J.
731 Metam. Geology 30, 703-722.

732 Gueydan, F., Leroy, Y.M., Jolivet, L., Agard, P., 2003. Analysis of continental midcrustal strain
733 localization induced by microfracturing and reaction-softening. Journal of Geophysical
734 Research 108/B2, 2064. doi:10.1029/2001JB000611.

735 Herwegh, M., Berger, A., Wehrens, P., Baumberger, R., Kissling, E., 2017. Large-Scale Crustal-Block-
736 Extrusion during late Alpine Collision. Nature Scientific Reports 7, 413-418.

737 Herwegh, M., Mock, S., Wehrens, P., Baumberger, R., Berger, A., Wangenheim, C., Glotzbach, C.,
738 Kissling, E., 2014., The Front of the Aar Massif, A Crustal-Scale Ramp Anticline?
739 Geophysical Research Abstracts, 17, EGU2015-11769.

740 Hess, J.C., Lippolt, H.J., 1994. Compilation of K-Ar measurements on HD-B1 standard biotite. in:
741 Odin G.S. (1994) : Phanerozoic time scale, Bull. Lias. Inform., IUGS subcom. Geochronol.,
742 12, Paris, 19-23.

743 Hobbs, B.E., Ord, A., Spalla, M.I., Gosso, G. & Zucali, M., 2010. The interaction of deformation and
744 metamorphic reactions. Geological Society, London, Special Publications, 332, 189–223.

745 Jäger, E., Kempter, E., Niggli, E., Wu?thrich, H., 1961. Biotit-Varietäten und Stilpnomelan im alpin
746 metamorph u?berprägten Mittagfluh-Granit, Aarmassiv. Schweiz. Min. Petr. Mitt. 41, 117-
747 126.

748 Kammer, A., 1989. Alpidische Verformung des aarmassivischen Nordrandes. Schweiz. Min. Petr. Mitt.
749 69, 37-53.

750 Keller, L.M., De Capitani, C., Abart, R., 2005. A quaternary solution model for white micas based on
751 natural coexisting phengite-paragonite pairs. J. Petrology 46, 2129-2144.

752 Kellett, D.A., Warren, C., Larson, K.P., Zwingmann, H., van Staal, C., Rogers, N., 2016. Influence of
753 deformation and fluids on Ar retention in white mica, Dating the Dover Fault, Newfoundland
754 Appalachians, Lithos, 254–255, 1-17, DOI: 10.1016/j.lithos.2016.03.003.

755 Kelley, S., 1988. The relationship between K-Ar mineral ages, mica grainsizes and movement on the
756 Moine Thrust Zone, NW Highlands, Scotland Journal of the Geological Society 145, 1-10.

757 Labhart, T.P., 1966. Mehrphasige Alpine Tektonik am Nordrand des Aarmassivs , Beobachtungen im
758 Druckstollen Trift-Speicherberg, Gadmental. der Kraftwerke Oberhasli AG. Eclogae geol.
759 Helv. 59, 803-830.

760 Labhart, T.P., 1977. Aarmassiv und Gotthardmassiv vol 63. Sammlung geologische Führer 63.
761 Gebruder Borntraeger Verlagsbuchhandlung,

762 Lanari P, Guillot S, Schwartz S, Vidal O, Tricart P, Riel N, Beyssac O, 2012. Diachronous evolution of
763 the alpine continental subduction wedge, evidence from P-T estimates in the Brianc¸onnais
764 Zone houille`re, France-Western Alps. J. Geodyn. 56–57, 39–54.

765 Lanari, P., 2012. P-T-e Micro-mapping in metamorphic rocks. Application to the Alps and the
766 Himalaya. Ph.D. Thesis, *University of Grenoble*, p. 544

767 Lanari, P., Engi, M., 2017. Local bulk composition effects on mineral assemblages, Reviews in
768 Mineralogy and Geochemistry, 38.

769 Lanari, P., Vidal, O., DeAndrade, V., Dubacq, B., Lewin, E., Grosch, E.G., Schwartz, S., 2014a,
770 XMapTools, A MATLAB-based program for electron microbe X-ray image processing and
771 geothermobarometry. Computers & Geosciences 62, 227-240.

772 Lanari, P., Rolland, Y., Schwartz S., Vidal, O., Guillot, S., Tricart, P., Dumont, T, 2014b. P-T-t
773 estimation of syn-kinematic strain in low-grade quartz-feldspar bearing rocks using

774 thermodynamic modeling and $^{40}Ar/^{39}Ar$ dating techniques, example of the Plan-de-Phasy
775 shear zone unit, Briançonnais Zone, Western Alps. Terra Nova, 26, 130-138.

776 Lanari, P., Wagner, T., Vidal, O., 2014c. A thermodynamic model for di-trioctahedral chlorite from
777 experimental and natural data in the system MgO-FeO-Al2O3-SiO2-H2O. Applications to P-T
778 sections and geothermometry. Contributions to Mineralogy and Petrology, 167, 968.

779 Livi, K.J.T., Veblen, D.R., Ferry, J.M., Frey, M., 1997. Evolution of 2:1 layered silicates in low-grade
780 metamorphosed Liassic shales of Central Switzerland. Journal of Metamorphic Geology 15,
781 323-344.

782 Mancktelow, N., Zwingmann, H., Campani, M., Fügenschuh, B., Mulch, A., 2015. Timing and
783 conditions of brittle faulting on the Silltal-Brenner Fault Zone, Eastern Alps (Austria). Swiss
784 Journal of Geosciences, 108, 305-326. DOI: 10.1007/s00015-015-0179-y

785 Mancktelow, N., Zwingmann, H., Mulch, A., 2016. Dating of fault gouge from the Naxos detachment
786 (Cyclades, Greece). Tectonics - doi: 10.1002/2016TC004251.

787 Markley, M. J., Teyssier, C., Cosca, M. A., Caby, R., Hunziker, J.-C. & Sartori, M., 1998. Alpine
788 deformation and 40Ar/39Ar geochronological synkinematic white mica in the Siviez-
789 Mischabel Nappe, western Pennine Alps, Switzerland. Tectonics, 17, 407–425.

790 McAleer, R.J., Bish, D.I., Kunk, M.J., Sicard, K.R, Valley, P.M., Walsh, G.J, , Wathen, B.J., Wintsch,
791 R.P., 2017. Reaction softening by dissolution–precipitation creep in a retrograde greenschist
792 facies ductile shear zone, New Hampshire, USA. Journal of metamorphic Geology, 35, 95–
793 119.

794 McDougall, I., Harrison, T,M., 1999. Geochronology and Thermochronology by the 40Ar/39Ar
795 Method. Oxford University Press, Oxford

796 Moore, D.M., Reynolds, R.C., 1989. X-ray Diffraction and the Identification and Analysis of Clay
797 Minerals 378. Oxford university Press Oxford

798 Mulch, A., Cosca, M., Handy, M., 2002. In-situ UV-laser $^{40}Ar/^{39}Ar$ geochronology of a micaceous
799 mylonite, an example of defect-enhanced argon loss. Contributions to Mineralogy and
800 Petrology 142, 738-752.

801 Niggli, E., Niggli, C., 1965. Karten der Verbreitung einiger Mineralien der alpidischen Metamorphose
802 in den Schweizer Alpen, Stilpnomelan, Alkali-Amphibol, Chloritoid, Staurolith, Disthen,
803 Sillimanit. Eclogae geol. Helv. 58, 335-368.

804 Odin, G.S. and 35 collaborators 1982. Interlaboratory standards for dating purposes. in: ODIN, G.S.
805 (editor) Numerical Dating in Stratigraphy. Part 1. John Wiley & Sons, Chichester, 123-148.

806 Parra, T., Vidal, O., Jolivet, L., 2002. Relation between deformation and retrogression in blueschist
807 metapelites of Tinos island, Greece. evidenced by chlorite-mica local equilibria. Lithos 63,
808 41–66.

809 Pleuger, J., Mancktelow, N., Zwingmann, H., Manser, M., 2012. K–Ar dating of synkinematic clay
810 gouges from Neoalpine faults of the Central, Western and Eastern Alps Tectonophysics 550–
811 553, 1-16.

812 Putnis A., Austrheim, H., 2013. Mechanisms of metasomatism and metamorphism on the local mineral
813 scale: The role of Dissolution-Reprecipitation during mineral re-equilibration. In D.E. Harlov
814 and H. Austrheim, Eds., Metasomatism and the Chemical Transformation of Rock, p. 141-
815 170. Springer.

816 Putnis, A., 2002. Mineral replacement reactions, from macroscopic observations to microscopic
817 mechanisms. Mineralogical Magazine, 66, 689-708.

818 Reichenbach, H., Rich, C., 1969. Potassium release from muscovite as influenced by particle size Clays
819 and Clay Minerals 17, 23-29.

820 Rolland, Y., Cox, S.F., Corsini, M., 2009. Constraining deformation stages in brittle-ductile shear
821 zones from combined field mapping and 40Ar/39Ar dating, The structural evolution of the
822 Grimsel Pass area, Aar Massif, Swiss Alps. Journal of Structural Geology 31, 1377-1394

823 Rossi, M., Rolland , Y., 2014. Stable isotope and Ar/Ar evidence of prolonged multiscale fluid flow
824 during exhumation of orogenic crust: Example from the Mont Blanc and Aar Massifs (NW
825 Alps). Tectonics, 33, doi:10.1002/2013TC0034

826 Sanchez G et al., 2011. Dating low-temperature deformation by 40Ar/39Ar on white mica, insights
827 from the Argentera-Mercantour Massif, SW Alps. Lithos 125, 521-536.

828 Schaltegger, U., 1993. The evolution of the polymetamorphic basement in the Central Alps unravelled
829 by precise U-Pb zircon dating Contributions to Mineralogy and Petrology 113, 466-478.

830 Schaltegger, U., 1994. Unravelling the pre-Mesozoic history of Aar and Gotthard massifs, Central
831 Alps. by isotopic dating, a review , The pre-Alpine crustal evolution of the Aar-, Gotthard-
832 and Tavetsch massifs. Schweizerische mineralogische und petrographische Mitteilungen 74,
833 41-51.

834 Schaltegger, U., Abrecht, J., Corfu, F., 2003. The Ordovician orogeny in the Alpine basement,
835 constraints from geochronology and geochemistry in the Aar Massif, Central Alps. Swiss
836 Bulletin of Mineralogy and Petrology 83, 183-239.

837 Scheffer, C., Vanderhaeghe, O., Lanari, P., Tarantola, A., Ponthus, L., Photiades, A., France, L., 2016.
838 Syn- to post-orogenic exhumation of metamorphic nappes, Structure and thermobarometry of
839 the western Attic-Cycladic metamorphic complex, Lavrion, Greece. Journal of Geodynamics
840 96, 174–193.

841 Schneider, S., Hammerschmidt, K., Rosenberg, C.L., 2013. Dating the longevity of ductile shear zones,
842 Insight from $^{40}Ar/^{39}Ar$ in situ analyses. Earth and Planetary Science Letters 369, 43-58.

843 Shea, W. T., and A. K. Kronenberg, 1992., Rheology and deformation mechanisms of an isotropic
844 mica schist. J. Geophys. Res., 97, 15201–15237. DOI:10.1029/92JB00620.

845 Solum, J.G., van der Pluijm, B.A., Peacor, D.R., 2005. Neocrystallization, fabrics and age of clay
846 minerals from an exposure of the Moab Fault, Utah. Journal of Structural Geology 27, 1563-
847 1576.

848 Solum, J. G., Davatzes, N. C., Loaner, D. A., 2010. Fault-related clay authigenesis along the Moab
849 Fault: implications for calculations of fault rock composition and mechanical and hydrologic
850 fault zone properties. Journal of Structural Geology, 32, 1899–1911.

851 Sperner, B., Jonckheere, R., Pfänder, J.A., 2014. Testing the influence of high-voltage mineral
852 liberation on grain size, shape and yield, and on fission track and 40Ar/39Ar dating Chemical
853 Geology 371, 83-95.

854 Stalder, H.A., 1964. Petrographische und mineralogische Untersuchungen im Grimselgebiet, mittleres
855 Aarmassiv., PhD Thesis, University of Bern.

856 Steck, A., 1968. Die alpidischen Strukturen in den Zentralen Aaregraniten des westlichen Aarmassivs.
857 Eclogae Geologicae Helvetiae 61, 19-48.

858 Steck, A., and Burri, G., 1971. Chemismus und Paragenesen von Granat aus Granitgneisen der
859 Grünschiefer- und Amphibolitfazies der Zentralalpen, Schweiz. Mineral. Petrogr. Mitt. 51,
860 534-536.

Steiger, R., Jäger, E., 1977. Submission on geochronology, Convention on the use of decay constants in geo-and costoochronology, Earth Planet Sei Letters 86, 359-362.

Torgersen, E., Viola, G., Zwingmann, H., Henderson, I.C.H., 2015. Inclined illite K-Ar age spectra in brittle fault gouges. Terra Nova, 27, 106-113. doi: 10.1111/ter.12136

Trincal, V., Lanari, P., 2016. Evidence of Al-free di-trioctahedral substitution in chlorite and a ferri-sudoite end-member. Clay Minerals, 51, 675-689.

van der Pluijm, B.A., Hall, C.M., Vrolijk, P.J., Pevear, D.R., Covey, M.C., 2001. The dating of shallow faults in the Earth's crust. Nature 412, 172-175.

Vidal, O., Lanari, P., Munoz, M., Bourdelle, F., de Andrade, V., 2016. Temperature, pressure, oxygen-activity conditions of chlorite formation. Clay Minerals, 51, 615-633.

Vidal, O., Parra, T., 2000. Exhumation of high pressure metapelites obtained from local equilibria for chlorite phengite assemblage. Geol Mag 35, 139–161.

Villa, I.M., 1998. Isotopic closure. Terra Nova 10, 42-47.

Villa, I.M., Bucher, S., Bousquet, R., Kleinhanns, I.C., Schmid, S.M., 2014. Dating Polygenetic Metamorphic Assemblages along a Transect across the Western Alps. Journal of Petrology 55, 803-830.

Villa, I.M., Hanchar, J.M., 2013. K-feldspar hygrochronology. Geochimica et Cosmochimica Acta, 101, 24-33.

Viola, G., Scheiber, T., Fredin, O., Zwingmann, H., Margreth, A., Knies, J., 2016. Deconvoluting complex structural histories archived in brittle fault zones. Nature communications, 7, 13448. DOI: 10.1038/ncomms13448 |

Viola, G., Zwingmann, H., Mattila, J., Käpyaho, A., 2013. K/Ar illite age constraints on the Proterozoic formation and reactivation history of a brittle fault in Fennoscandia Terra Nova 25, 236-244.

Wehrens P, Baumberger R, Berger A, Herwegh M, 2017. How is strain localized in a mid-crustal basement section? Spatial distribution of deformation in the Aar massif, Switzerland. Journal of Structural Geology 94, 47-67.

Wehrens, P., Berger, A., Peters, M., Spillmann, T., Herwegh, M., 2016. Deformation at the frictional-viscous transition: Evidence for cycles of fluid-assisted embrittlement and ductile deformation in the granitoid crust. Tectonophysics, 693A, 66-84.

Wintsch, R., 1985. The possible effects of deformation on chemical processes in metamorphic fault zones. In, Metamorphic Reactions, ed. Thompson, A., & Rubie, D.., pp. 251– 268, Springer, New York, NY.

Zwingmann, H., 2014. K-Ar/^{40}Ar/^{39}Ar dating - Clays and Glauconites. - In Rink, W.J., Thompson, J.W., Eds.. Encyclopedia of Scientific Dating Methods, Springer-Verlag, Berlin-Heidelberg.

Zwingmann, H., Berger, A., Eggenberger, U., Todd, A., Herwegh, M., in review., Testing high-voltage electrical pulses in disintegrating clay-stones for isotopic and mineralogical studies: An example using Opalinus clay. Clays and Clay minerals.

Zwingmann, H., Mancktelow, N., 2004. Timing of Alpine fault gouges Earth and Planetary Science Letters 223, 415-425 doi, 10.1016/j.epsl.2004.04.041

Zwingmann, H., Mancktelow, N., Antognini, M., Lucchini, R., 2010. Dating of shallow faults, New constraints from the AlpTransit tunnel site, Switzerland. Geology 38, 487-490

903 Zwingmann, H., Offler, R., Wilson, T., Cox, S., 2004. K–Ar dating of fault gouge in the northern
904 Sydney Basin, NSW, Australia—implications for the breakup of Gondwana Journal of
905 Structural Geology 26, 2285-2295.

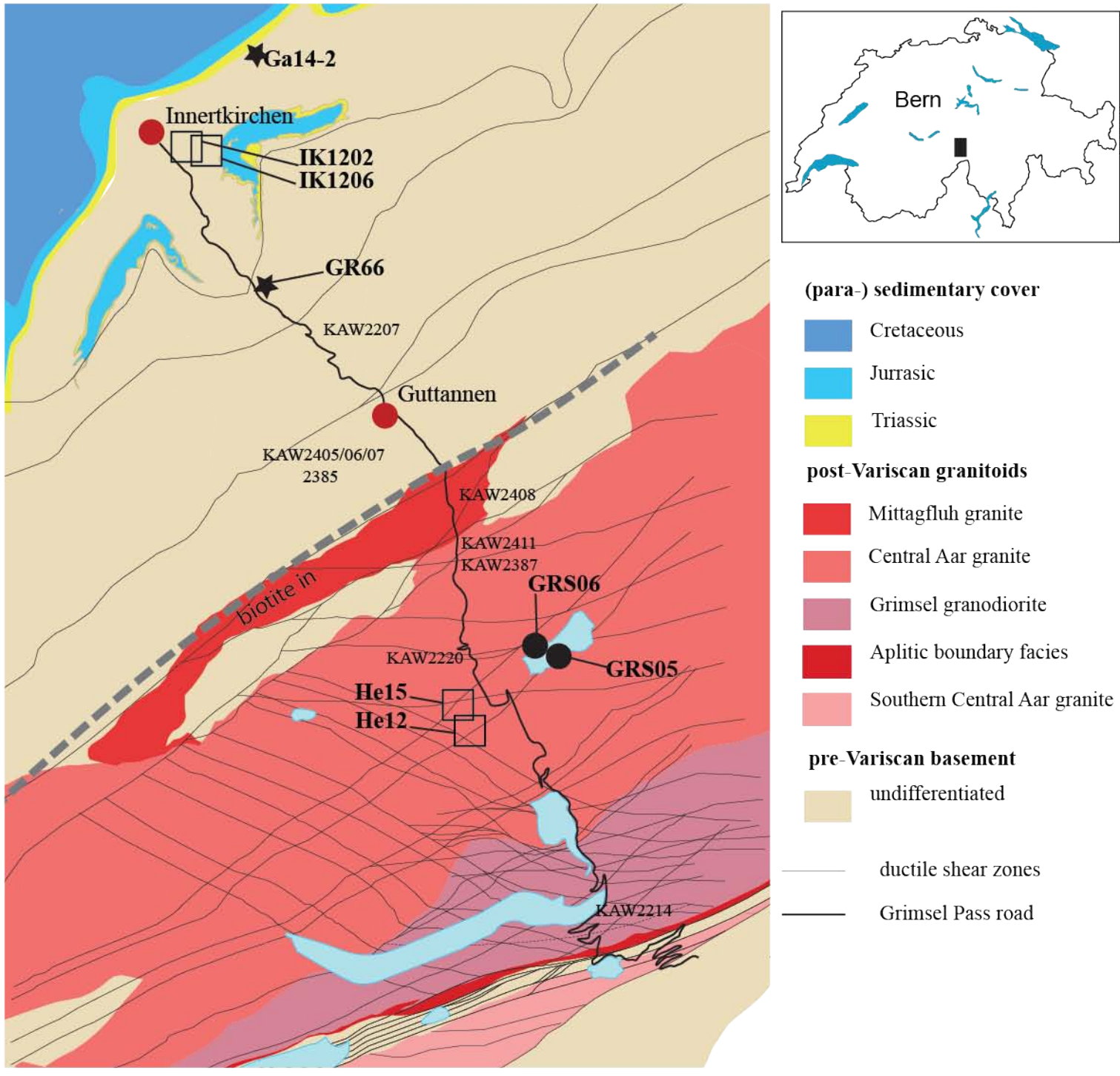

Figure 1:

Map of the Haslital with the Innertkirchen area to the north and the Gelmersee area in the south. Indicated are the surface locations and the tunnels where samples were taken. Also the main ductile shear zones are indicated (Baumberger 2015; Wehrens et al. 2017).

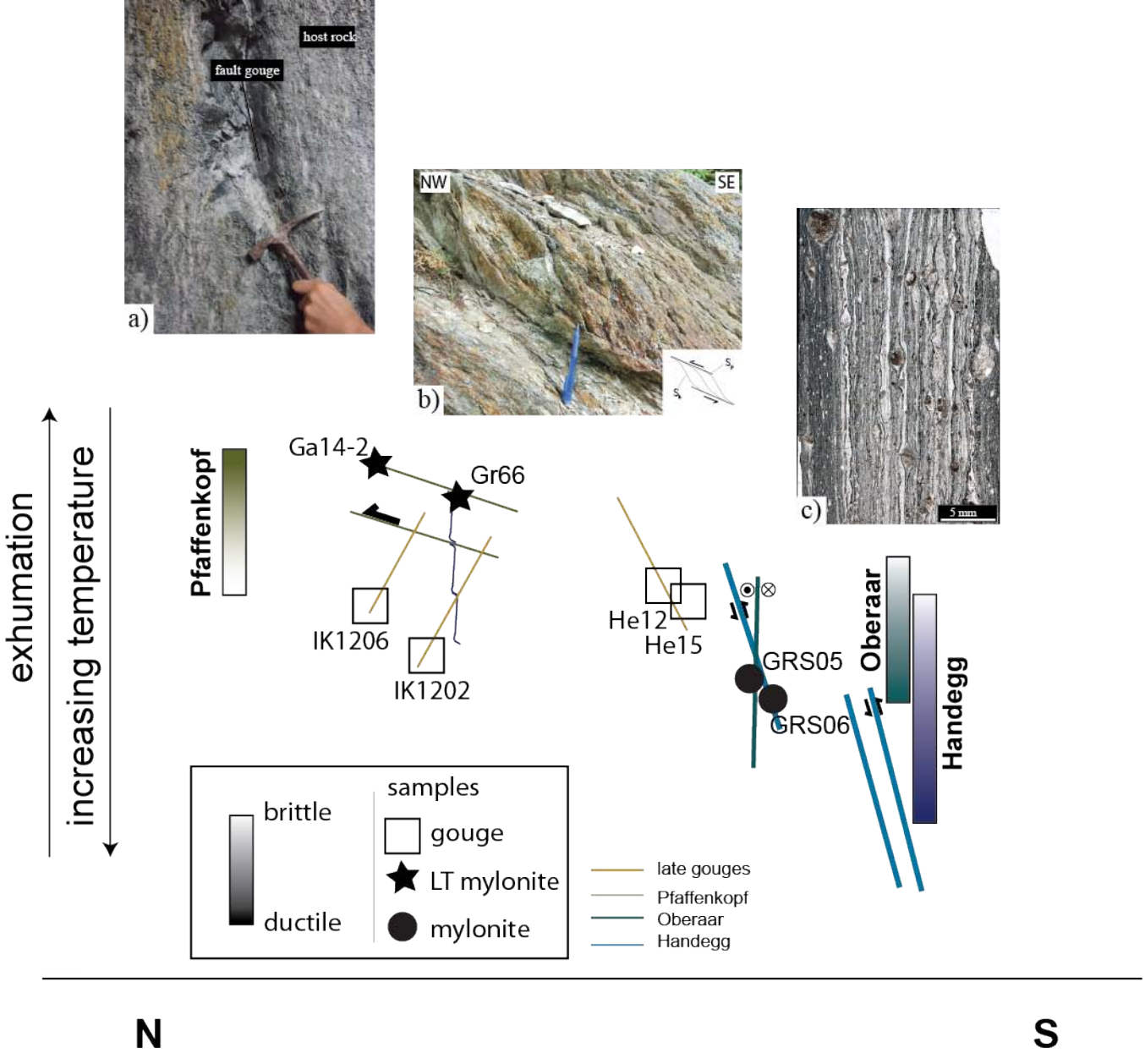

Figure 2:
Sketch of structural evolution and the selected samples along a N-S section along the Haslital. (a) Photo of outcrop showing the 10 cm wide fault gouge (b) Outcrop showing the Handegg foliation (Sh) and the Pfaffenchopf foliation (Sp), inset (lower right corner) shows the geometric relation. (c) Micrograph showing the mylonitic fabric of the intermeidate T mylonites. (d) Sketch indicating the shear zone orientations and the main conditions of deformation. Note the colors of the Handegg, Oberaar and Pfaffenkopf phase are shown in the orientaiton and the type of deformation.

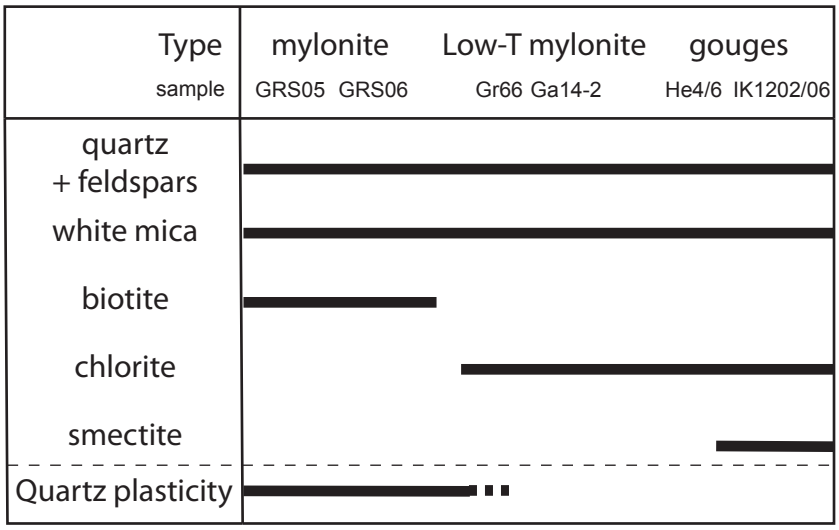

Figure 3:

Mineraldistribution in the analysed tectonites.

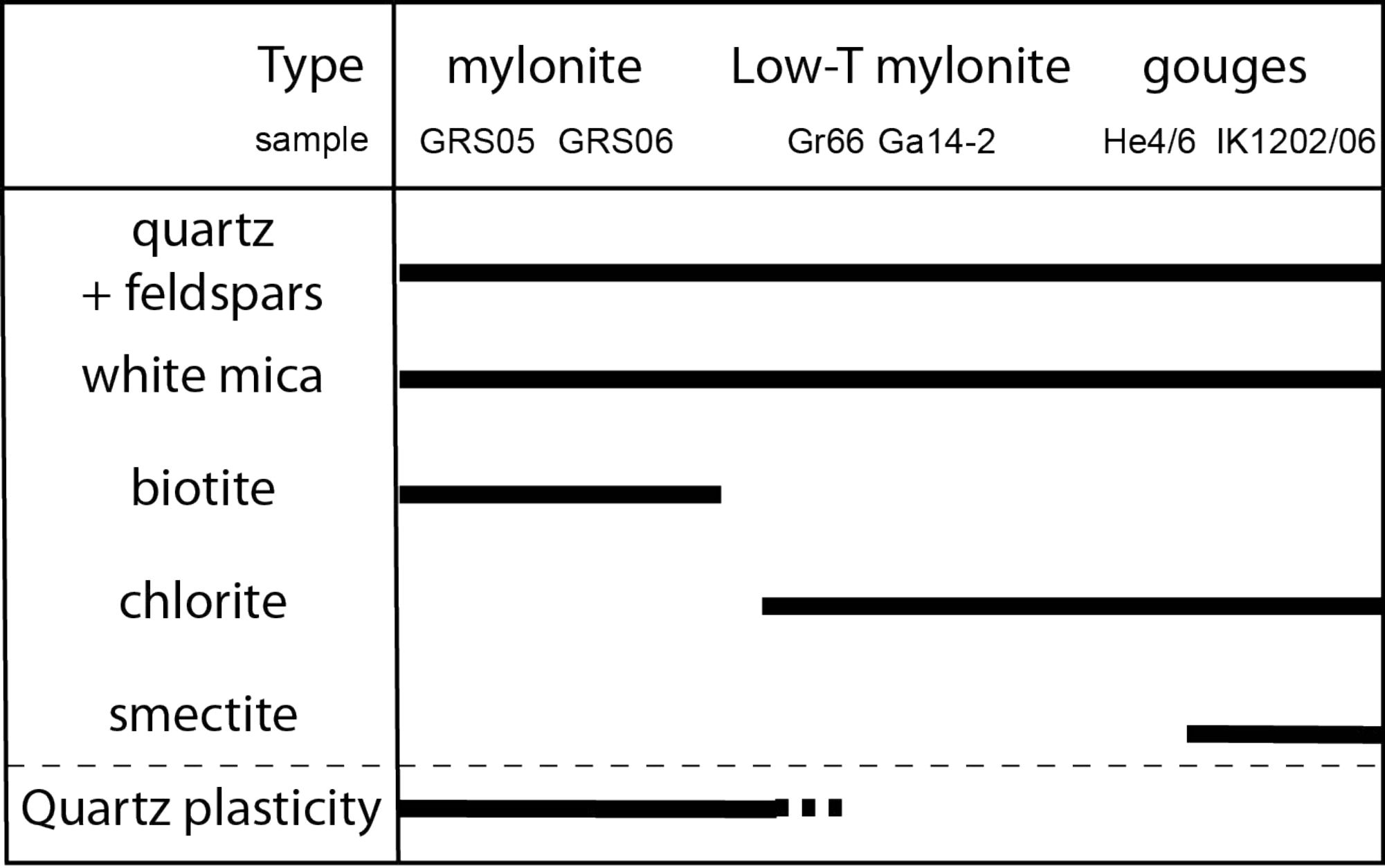

Figure 3:

Mineraldistribution in the analysed tectonites.

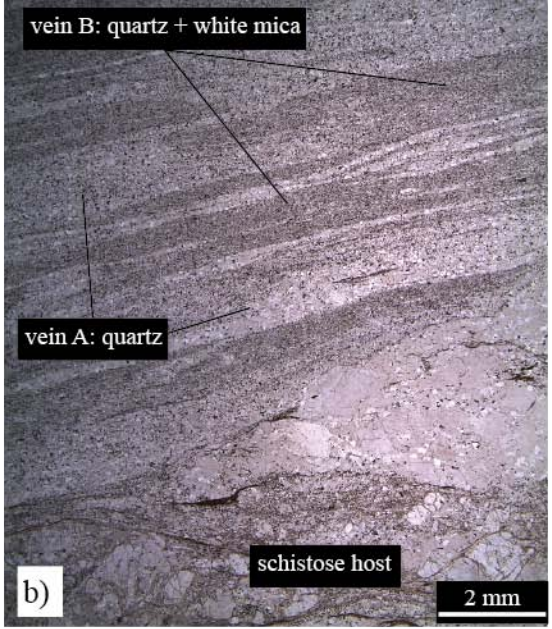

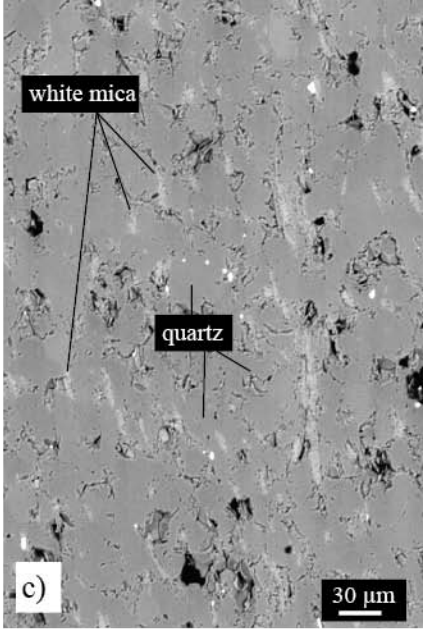

Figure 4:
(a) Hand specimen of sample GRS06 again showing the mylonitized monomineralic quartz veins (vein A) and quartz-mica bands (vein B) within the weakly schistose host. (b) Micrograph of GRS06 showing in the bottom of the image weakly schistose granitoid. In the top half of the image the quartz and white mica veins and pure quartz veins are visible. (c) Electron backscatter image of the white mica quartz vein. Note the aligned and homogeneously distributed white mica grains with sizes down to a few µm.

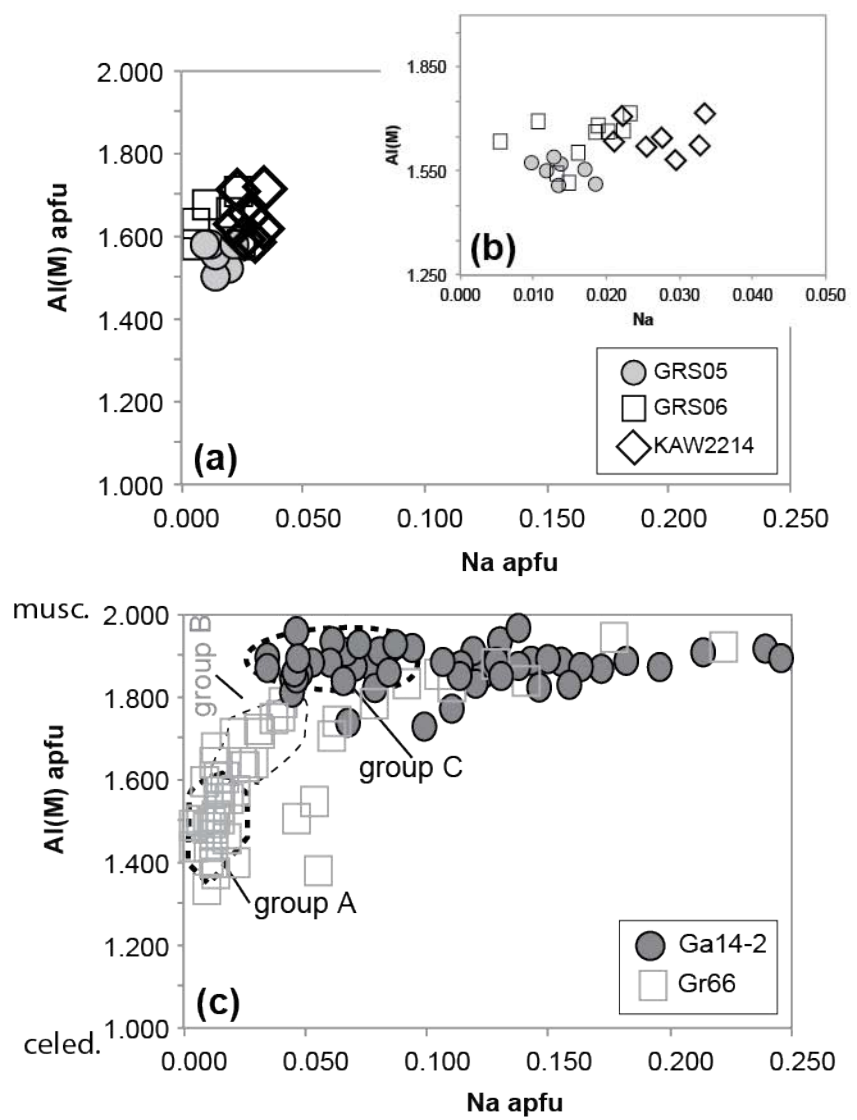

Figure 5:

Mineralchemical data in Al (apfu) versus Na (apfu) diagrams. The Al is recalculated on the M-site. (a) data from the mylonites. Sample KAW2214 is from the south and for comparison only (see Table 1). (b) details of part (a). (c) data from the low-T mylonites (Gr66, Ga14-2).

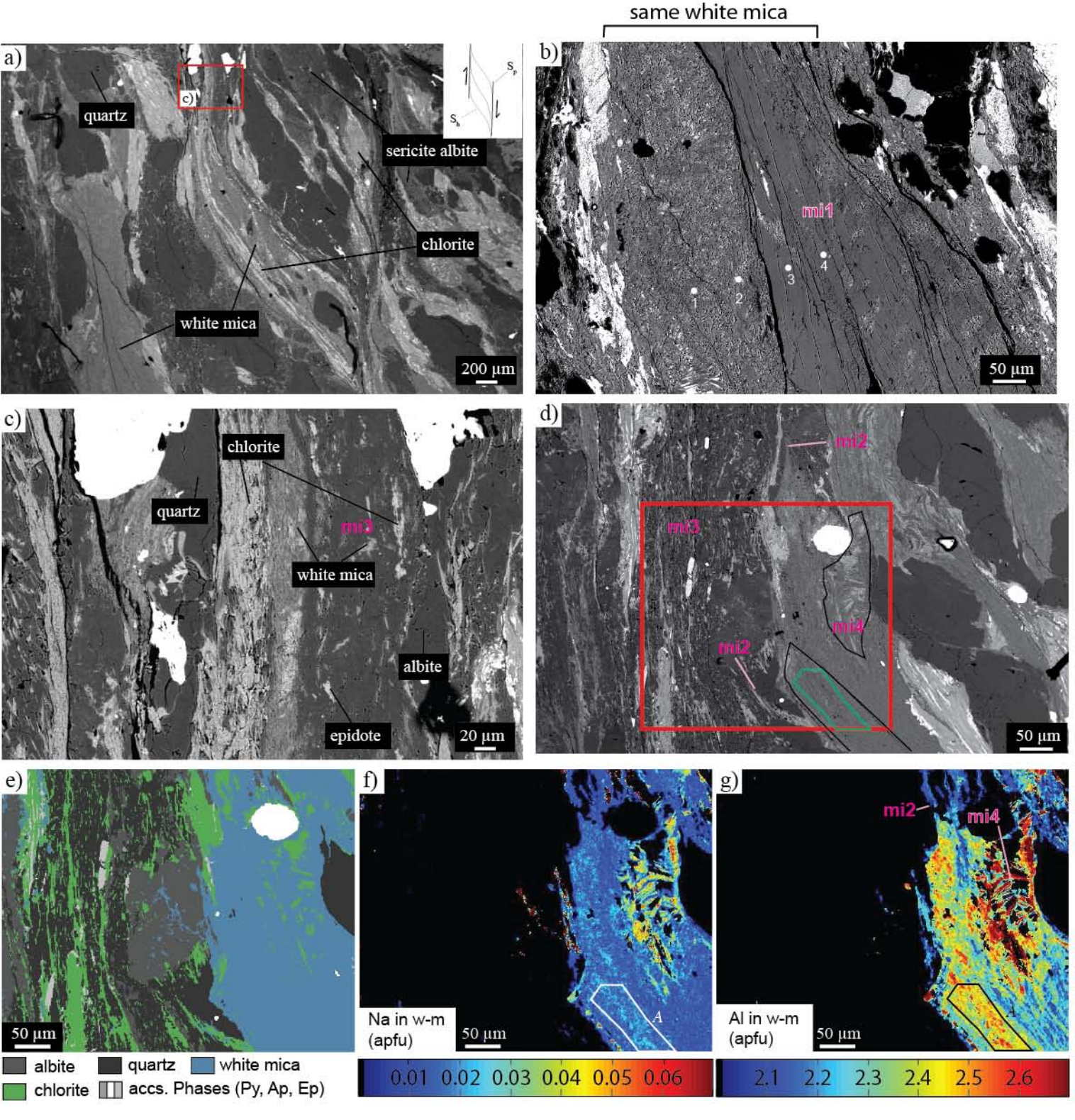

Figure 6:

Microstructures and quantitative maps of sample Gr66 (a-d) Backscatter electron images showing the different textures. (a) overview showing the the different planar fabrics; (c) zoom in of (a) showing the newly formed white mica in the Sp with a grain size ~5µm. (b) large grain of white mica, which is surrounded by fine grained material. Analytical points are given. (d) bending and recrystallisation of white mica into the Sp. Red angular is the position of quantitative mapping shown in (e-g). (e) phase distribution of the map (f) Na in white mica (unit: atoms per formula unit). (g) Al in white mica (apfu). The different micrsostructural types (mi1-mi5) are marked in the different images.

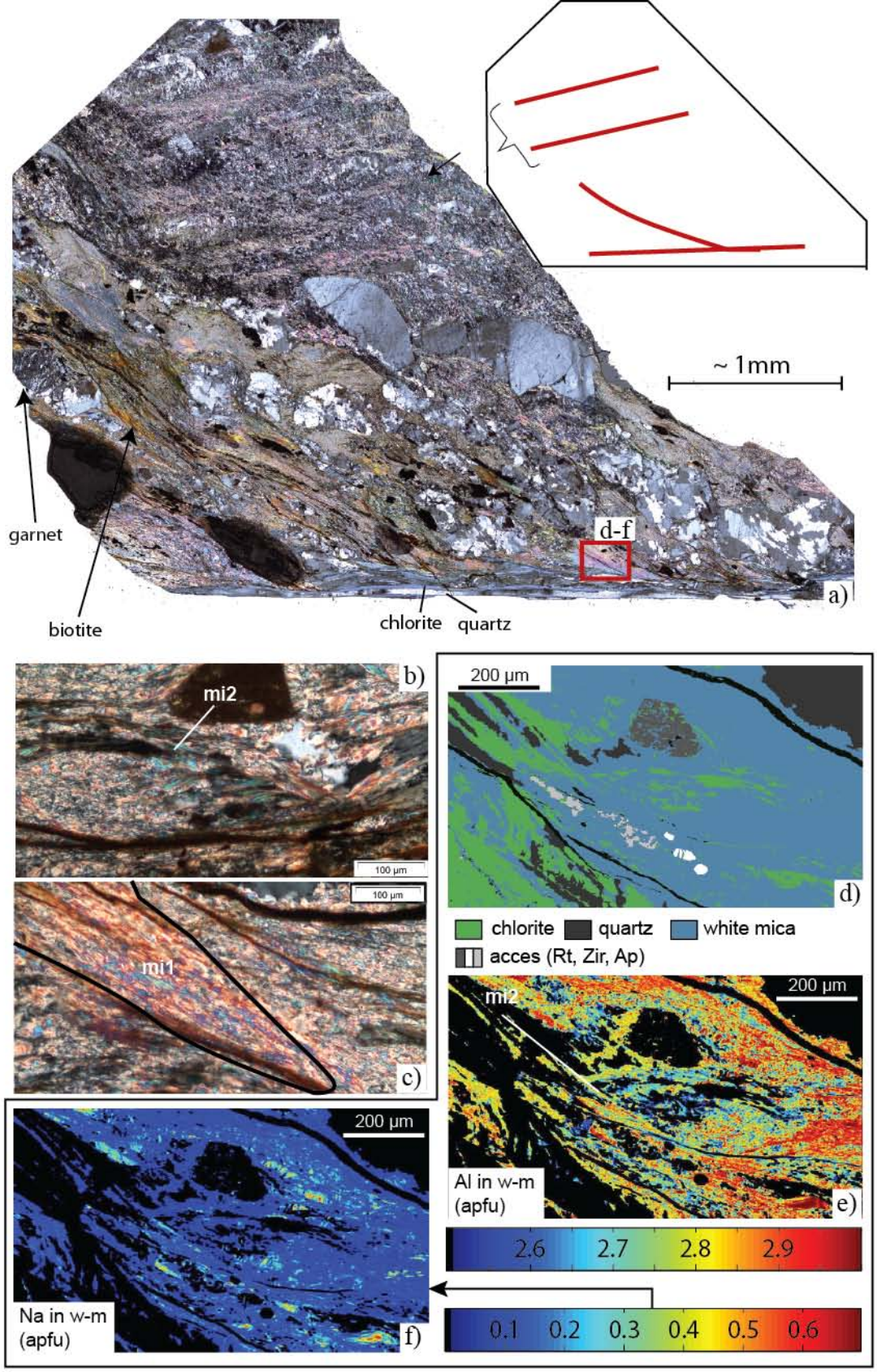

Figure 7:

Microtextural map of sample Ga14-2. (a) optical microphotograph of the complete section Red angular is the posiiton of quantitative mapping shown in (b-f). (b) , (c) . (d) phase distribution of the map (e) Al in white mica distribution (unit: atoms per formula unit, apfu). (f) Na in white mica (apfu). The pixels in red are paragonite, whereas the pixels in green (Na = 0.3-0.5 apfu) are mixing analysis between K-white mica and paragonite.

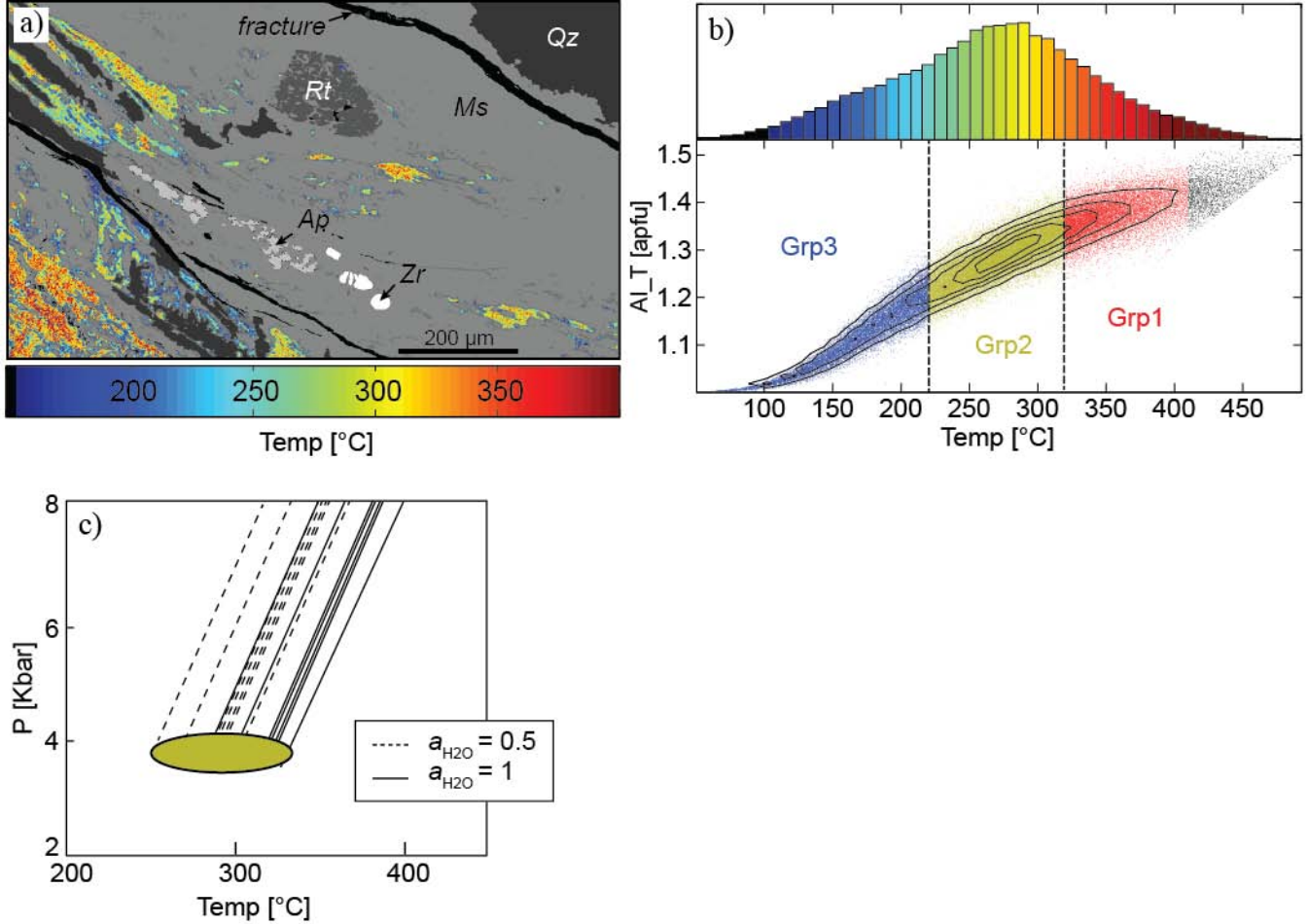

Figure 8:

Chlorite and white mica thermobarometry. (a) Temperature map of chlorite calculated using the calibration of Lanari et al. (2014) at a fixed pressure of 5 kbar. (b) The Temperatures are reported again the amount of Al in tetrahedral position (Al_T) expressed in atom per formula unit (apfu). Three groups are distinguished based on the temperature map and they are reported in (b). The colors of the bars of the temperature histogram are based on the colormap of the temperature map. (c) P-T equilibrium lines between white mica (mi2, see Fig. 7), quartz and water calculated for aH2O = 1 (continuous lines) and aH2O = 0.5 (dashed lines) using the callibration of Dubacq et al. (2010). The green elipse show the best intersection between the chlorite temperature (Grp2, see text) and the white mica equilibrium lines.

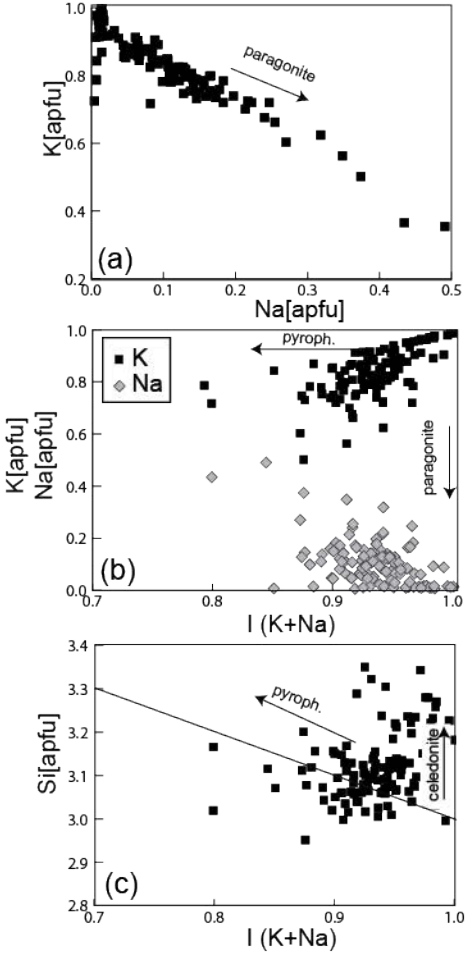

Figure 9:
Mineralchemistry of white mica in low-T mylonites. (a) Na versus K per formuila unit, the paragonite exchange vector is indicated. (b) amount of K+Na versus K and versus Na; (c) K+Na versus Si content. The pyrophyllite vector and limits are indicated.

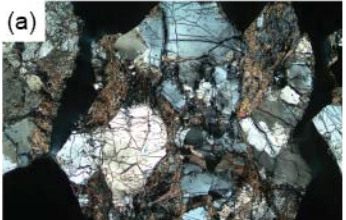

K/Ar age: <0.8µm ~33 Ma

K/Ar age: <0.8µm ~19 Ma

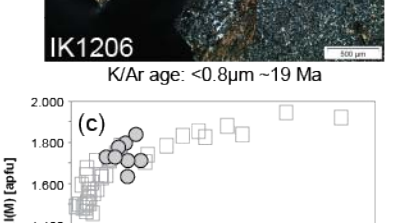

Figure 10:

The connection of fragments in gouges and their evolution. (a+b) Microphotograph of the two southern investigated gouges. Note the different recrystallisation of the quartz and the related apparent ages. (c) Microprobe data of the micas inside the fragments of sample IK1206.

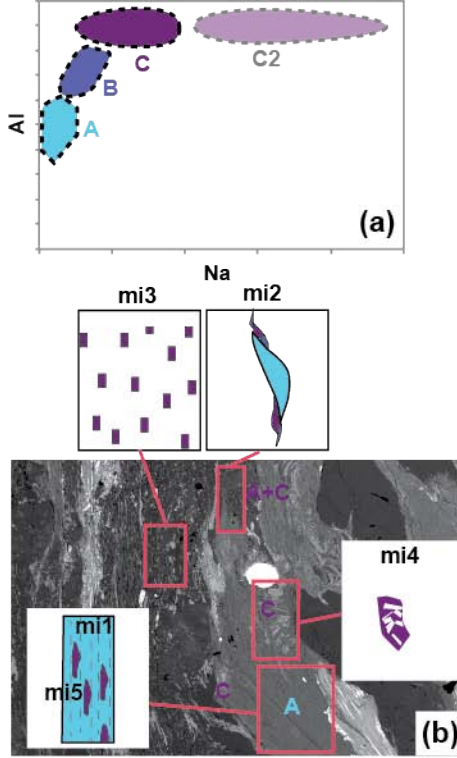

Figure 11:

Relationship between microstructural- (*mi1-mi5*) and chemical groups (A, B.C). (a) Scheme of the mica composition, simplifed from figure 5; (b) microphotgraph from figure 6 with schematic microstructural groups (Table 7). Capital letters indicate the chemcial mica groups (see figure 6f+g).

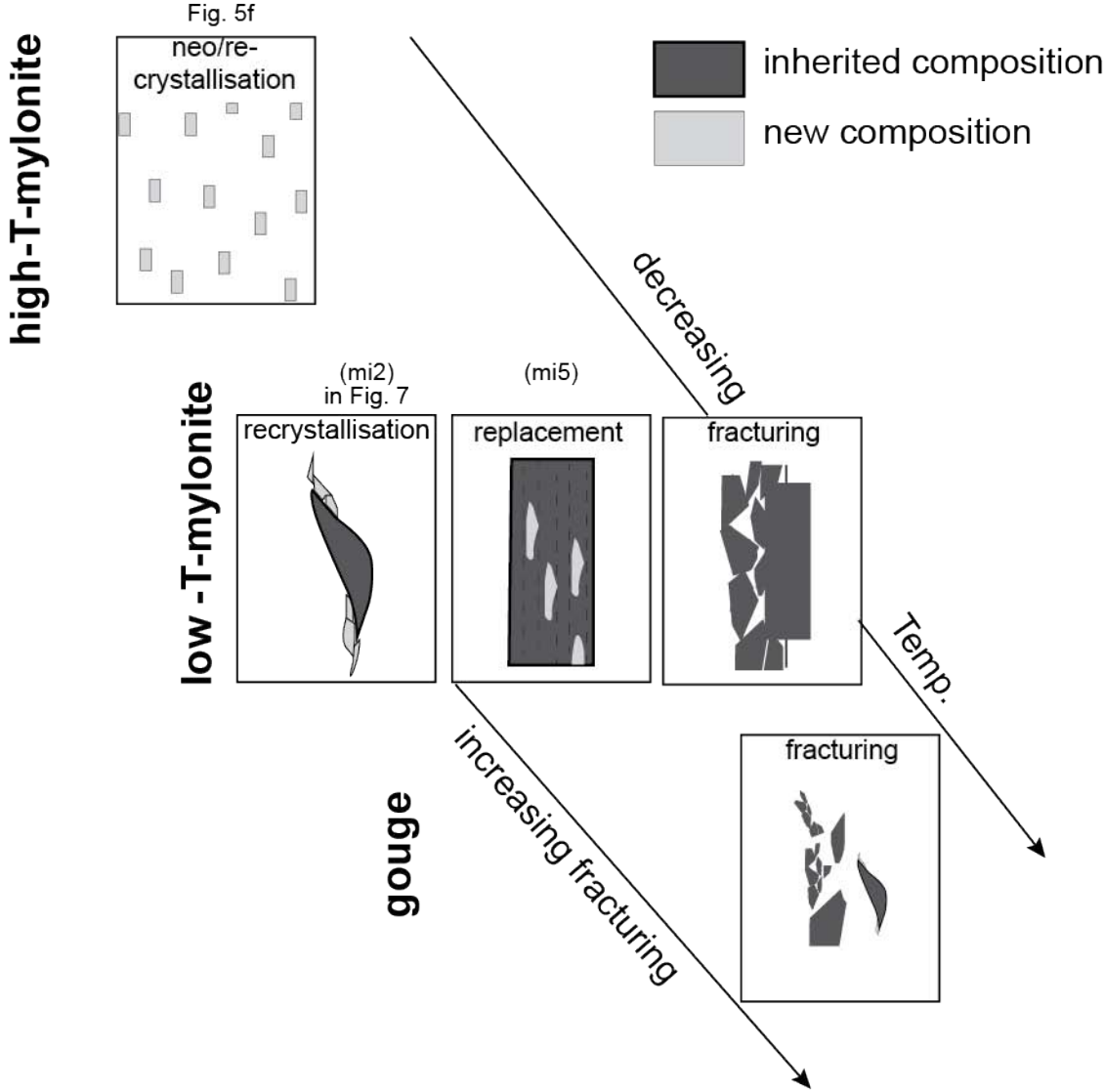

Figure 12:

Sketch of different microstructures described along the temperature evolution

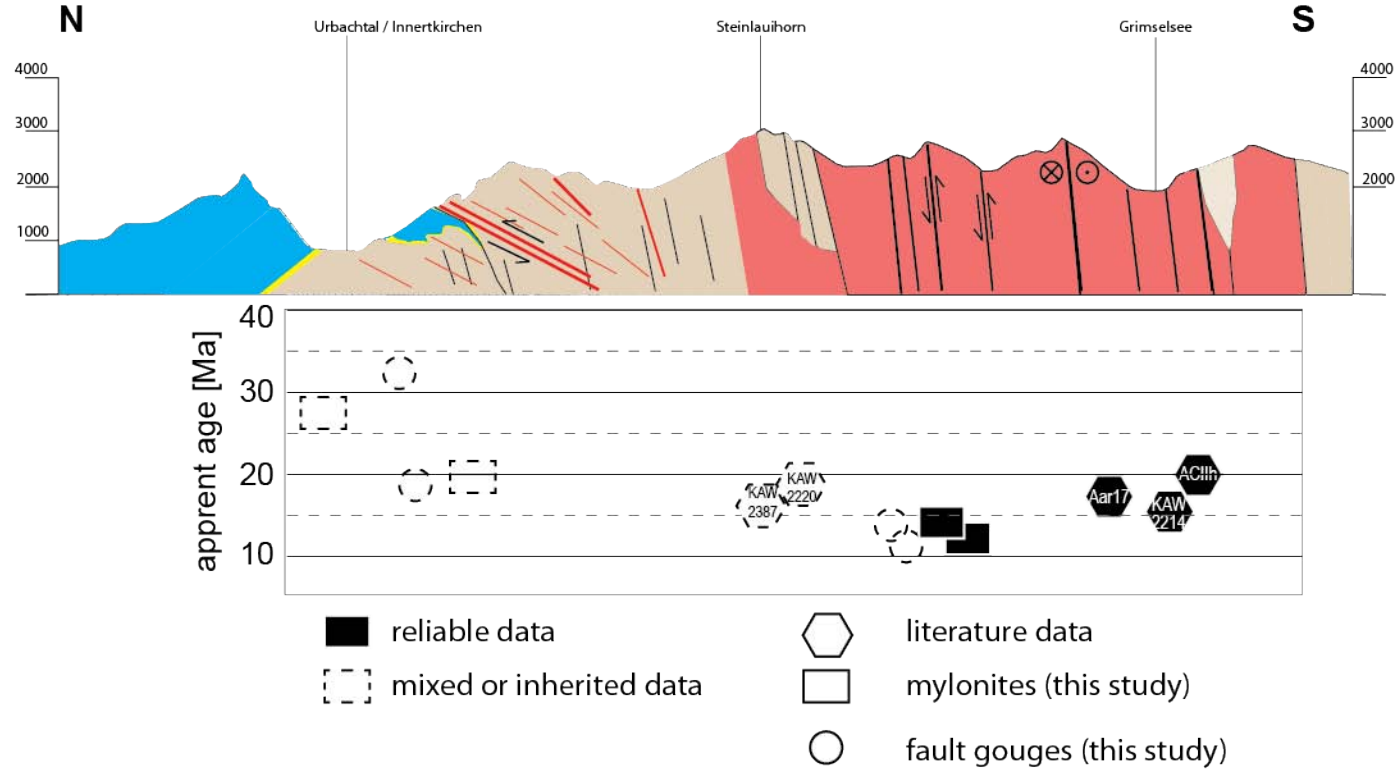

Figure 12:

Distribution of white mica Ar-ages along the Halsital. Data are from Table 1.

Table 1: Available K/Ar data sorted from N to S and coordinates for the investigated samples

				biotite	white mica		
	Sample	coordinates	rock-type	K/Ar	K/Ar age smallest fraction	Ar age oldest age	Reference
	Ga14-2	670190 176980	B		27±0.5	37±0.8	this study
N	KAW2207	661631 170978	D	246±3			D86
	Ik1202	661316 172478	C		33±0.7	37±0.7	this study
	Ik1206	661254 172514	C		19±0.4	21±0.4	this study
	Gr66	662470 169634	B		20±0.4	40±0.8	this study
	KAW2404	664131 168058	D	171±3			D86
	KAW2385		D	78±2		~180	D86
-	KAW2407	665971 166358	D	112±2			D86
	KAW2408	666200 166180	E	54±1			D86
	KAW2387	666000 164400	E			16±1	D86
	KAW2220	666400 163000	E	23±0.5		18±1	D86
	He12	666470 161622	C		12±0.3	11±0.3	this study
	He15	666362 161794	C		-	14±0.4	this study
	GRS05	668125 162697	A		12±0.3		this study
	GRS06	667629 162940	A		14±0.3		this study
	Aar17	667900 160450	E			17±0.1	C08
	KAW2214	668900 158500	E	19±0.5		15±1	D86
	ACIIh	668500 158400	B			19±0.1	C08
	Aa0351	668810 157290	B			14±0.1	R09
S	S123	664240 155480	B			13±0.1	R09

A: mylonite, B: low temperature-mylonite, C: fault gouge, D: basement gneiss, E. granitic gneiss
D86: Dempster 1986; C08: Challandes et al. 2008; R09: Rolland et al. 2009

Table 2: Overview of the separation and analytical methods for each sample and fraction

Sample	grain size fraction (µm)	Selfrag	Grain-size separat.	Mineralogy
GRS05	2- 6	x	C	X
GRS05	6- 10	x	A	X
GRS06	2- 6	x	C	X
GRS06	6- 10	x	A	X
GRS06	10- 20	x	A	X
GRS06	63- 500	x	p	TS
GR66	2- 6	x	C	X
GR66	63- 500	x	P	TS
Ga14-2	sep.		P	TS
Ga14-2	2-6	x	A	TS
Ga14-2	2-0.8	x	A	TS
Ga14-2	<0.8	x	A	TS
He12	< 0.8		C	X,G,H
He12	0.8- 2		C	X,G,H
He12	2- 5		C	X,G,H
He15	< 0.8		C	X,G,H
He15	0.8- 2		C	X,G,H
He15	2- 5		C	X,G,H
Ik1202	< 0.8		C	X,G,H
Ik1202	0.8- 2		C	X,G,H
Ik1202	2- 5		C	X,G,H
Ik1206	< 0.8		C	X,G,H
Ik1206	0.8- 2		C	X,G,H
Ik1206	2- 5		C	X,G,H

Abbreviations: C: centrifuge, A: Atterberg, P: hand-picked, X: XRD, G: glycolated, H: Heat treated, TS: thin-section

Table 3: Standards measured during the course of this research

Standard ID	K [%]	Rad. 40Ar [mol/g]	Rad. 40Ar [%]	Age [Ma]	Error [Ma]	Error to reference [%]
GLO-154	6.55	1.1196E-09	94.35	95.96	1.49	+0.98
GLO-157	6.55	1.1093E-09	94.54	95.09	1.50	+0.06
HD-B1-121	7.96	3.3294E-10	90.46	23.97	0.37	-0.99
HD-B1-124	7.96	5.4850E-11	92.58	24.31	0.37	+0.41
HD-B1-125	7.96	3.3574E-10	91.97	24.17	0.36	-0.17

Airshot ID	40Ar/36Ar	+/-
AS116-AirS-1	295.69	0.36
AS117 AirS-1	296.86	0.31
AS118-AirS-1	295.17	0.56
AS120-AirS-1	295.55	0.29
AS121-AirS-1	296.96	0.24

Table 4: Representative white mica analyses

sample	KAW2214	KAW2214	GRS05	GRS06	Gr66	Ga14-2	Gr66	Ga14-2
					groupA	groupC	groupC	groupC2
SiO_2	47.17	47.44	45.97	48.22	50.19	45.68	47.41	45.85
TiO_2	0.04	0.04	0.17	0.05	0.04	bd	0.02	0.03
Al_2O_3	33.37	30.39	30.15	31.05	27.49	35.44	32.52	36.22
FeO	2.88	4.19	4.73	2.80	2.89	1.69	1.66	1.40
MnO	bd	0.16	1.00	bd	bd	0.01	0.04	0.03
MgO	0.94	1.88	2.05	2.78	2.98	0.94	1.95	0.49
CaO	0.08	bd	bd	bd	bd	bd	0.03	0.14
Na_2O	0.64	0.19	0.10	0.04	0.08	0.65	0.29	1.65
K_2O	10.97	11.45	11.68	11.69	11.48	10.26	10.63	8.22
sum	96.09	95.74	95.85	96.63	95.15	94.67	94.56	94.02

Table 5: Composition of the analyzed samples and grain size fractions. Note that the distinction between chlorite and smectite has only been made for the finest grain sizes of the gouges. The amount of each phase is estimated and indicated from minor to dominant with "x " to "xxxx" respectively. The "(x)" refers to a phase which could not unequivocally be determined.

Sample	grain size fraction (µm)	smectite	kaolinite	illite/ muscovite	biotite	quartz	k-feldpsar	albite	chlorite
GRS05	2- 6			xxx	xxx	xx	x	x	x
GRS05	6- 10			xxx	xxxx	xx	x	xx	x
GRS06	2- 6			xxx		xxx		xx	
GRS06	6- 10			xxx		xxx		xx	
GRS06	10- 20			xxx		xxxx		xx	
GRS06	63- 500			x					
He12	< 0.8	xxxx	x	xx			(x)		
He12	0.8- 2	xxx	x	xxx			(x)		
He12	2- 5	xx	x	xxxx			(x)		
He15	< 0.8			xx					x
He15	0.8- 2	xxxx	x	xx					
He15	2- 5	xxx	x	xxx					x
GR66	2- 6			xxx		xxx		x	xxxx
GR66	63- 500			x					x
Ik1202	< 0.8	xxx	xx	xxxx					x
Ik1202	0.8- 2	xx	xxx	xxxx					x
Ik1202	2- 5	xx	xxx	xxxx					x
Ik1206	< 0.8	xx	x	xxx				x	
Ik1206	0.8- 2	xx	x	xxxx				x	
Ik1206	2- 5	xx	x	xxxx				x	

Table 6: K-Ar data for all measured samples and fractions

Sample	tecto. group *	grain size fraction (µm)	K [%]	Rad. 40Ar [mol/g]	Rad. 40Ar [%]	Age [Ma]	Error [Ma]
GRS05	A	2- 6	5.31	1.1295E-10	82.18	12.2	0.3
GRS05	A	6- 10	5.80	1.1947E-10	81.74	11.8	0.2
GRS06	A	2- 6	5.16	1.2108E-10	87.79	13.5	0.3
GRS06	A	6- 10	4.39	1.0081E-10	92.18	13.2	0.3
GRS06	A	10- 20	4.61	1.0679E-10	89.83	13.3	0.3
GRS06	A	63- 500	6.65	1.5696E-10	94.72	13.6	0.3
He12	C	< 0.8	3.70	7.531E-11	34.15	11.7	0.3
He12	C	0.8- 2	4.55	1.0152E-10	40.95	12.8	0.3
He12	C	2- 5	5.23	1.0238E-10	34.66	11.3	0.3
He15	C	< 0.8	1.73	4.8349E-11	13.18	16.0	1.0
He15	C	0.8- 2	2.28	5.538E-11	35.65	14.0	0.5
He15	C	2- 5	3.62	9.0493E-11	31.96	14.4	0.4
Gr66	B	2- 6	5.80	2.0111E-10	91.38	19.9	0.4
Gr66	B	63- 500	3.55	2.4762E-10	88.62	39.8	0.8
Ga14-2	B	63- 500	3.18	1.989E-10	84.5	35.7	0.7
Ga14-2	B	2-6	4.89	3.178E-10	90.4	37.1	0.8
Ga14-2	B	2-0.8	5.03	2.629E-10	89.3	29.9	0.6
Ga14-2	B	<0.8	4.96	2.298E-10	86.6	26.5	0.5
Ik1202	C	< 0.8	6.30	3.6361E-10	84.98	33.0	0.7
Ik1202	C	0.8- 2	6.78	3.8377E-10	90.79	32.3	0.6
Ik1202	C	2- 5	6.49	4.1885E-10	89.35	36.8	0.7
Ik1206	C	< 0.8	6.68	2.1974E-10	74.26	18.9	0.4
Ik1206	C	0.8- 2	6.14	1.9892E-10	65.18	18.6	0.4
Ik1206	C	2- 5	6.76	2.4872E-10	77.51	21.1	0.4

A: mylonites, B: LT-mylonites, C: fault gouges

Table 7: Microstructural groups of low T mylonites

Group	description	grain size	Figure
mi1	relic grains	large	6
mi2	fractures/recrystallized	interm.	6, 7
mi3	precipitated in qtz/fsp matrix	small	6
mi4	pseudomorphs	variable	6, 7
mi5	replacement	large	6